

This work has been submitted to the IEEE for possible publication. Copyright may be transferred without notice, after which this version may no longer be accessible.

Unified Modeling and Structural Optimization of Multi-magnet Embedded Soft Continuum Robots for Enhanced Kinematic Performances

Zhiwei Wu[✉], Graduate Student Member, IEEE., Jiahao Luo[✉], Siyi Wei[✉], and Jinhui Zhang[✉].

Abstract—This paper presents a unified modeling and optimization framework to enhance the kinematic performance of multi-magnet embedded soft continuum robots (MeSCRs). To this end, we establish a differentiable system formulation based on an extended pseudo-rigid-body model. This formulation enables analysis of the equilibrium well-posedness and the geometry of the induced configuration under magnetic actuation. In particular, we show that the maximum controllable degrees of freedom of a MeSCR equal twice the number of embedded magnets. We subsequently develop a structural optimization framework based on differential geometry that links classical kinematic measures (e.g., manipulability and dexterity) to the configuration of embedded magnets. The resulting optimization condition reveals that improving local performance requires structurally modulating the spectrum of the configuration space metric to counteract its distortion. Closed-form solutions for optimal magnet configurations are derived under representative conditions, and a gradient-based numerical method is proposed for general design scenarios. Simulation studies validate the effectiveness of the proposed framework.

Index Terms—Magnetic soft continuum robots, pseudo-rigid-body modeling, kinematic performances, structure optimization.

I. INTRODUCTION

MAGNETICALLY actuated soft continuum robots have demonstrated significant potential in medical procedures such as vascular intervention and gastrointestinal examination [1]. Early designs typically embedded a single magnet at the distal end to enable basic magnetic manipulation [2]–[4]. However, the limited torque generated by such configurations restricts the controllable degrees of freedom (DoF) less than two [5], significantly constraining spatial maneuverability. Recent advances in magnetic materials and microfabrication have enabled the integration of multiple micro-magnets along the continuum body [6], [7], giving rise to multi-magnet embedded soft continuum robots (MeSCRs). These systems provide multiple distributed sources of actuation torque, substantially enhancing kinematic performance and expanding the design space. Various strategies have been proposed to exploit these capabilities, such as using movable magnets to enlarge reachable workspace [8], designing magnet layouts for multimodal deformation [9], [10], or inducing axial twisting via circumferential arrangements [11]. These efforts can be seen as structural design choices, analogous to tuning joint

orientations or link lengths in rigid manipulators to improve kinematic capabilities.

Despite this progress, the absence of a unified modeling framework for MeSCRs remains a major barrier. Unlike rigid-link manipulators, which benefit from well-established analytic tools for performance analysis and optimization, soft continuum robots lack a theoretical foundation that systematically links structure to kinematic function [12]. As a result, many mature strategies developed in rigid manipulators cannot be directly applied to MeSCRs, motivating the need for a new modeling paradigm that bridges this gap.

Current MeSCR modeling approaches typically fall into two categories: Cosserat rod models and pseudo-rigid-body (PRB) models. The Cosserat formulation provides high-fidelity representations and has been integrated with magnetic dipole actuation models for motion control [13], [14]. However, it requires solving boundary value problems derived from variational principles, making it analytically intractable and computationally intensive for iterative design. By contrast, the PRB model discretizes flexible structures into rigid links with elastic joints [15], [16], yielding a Lagrangian formulation analogous to rigid manipulators. This enables unified expressions for forward kinematics and simplifies equilibrium computation via unconstrained finite-dimensional optimization [17]. Early applications in single-magnet MeSCRs have demonstrated effective Jacobian-based control strategies [18], [19], and rank-based analysis has shown that such systems can control at most two DoF [5]. Recent work has extended the PRB formulation to multi-magnet settings [10], [20], preliminarily validating its capacity to simulate complex deformations.

Nevertheless, the PRB model also suffers from several inherent limitations. The choice of joint discretization entails a trade-off between modeling fidelity and computational cost. In particular, due to the lack of theoretical analysis on well-posedness, existing methods typically use numerical methods to analyze the multiplicity and jump phenomena of solutions [21]. Moreover, to our best knowledge, complete closed-form expressions for Jacobian (simplified expression can be found in [19], [20]) and Hessian matrices under multi-magnet configurations have not been established.

To address the limitations outlined above, the first part of this paper investigates an extended-pseudo-rigid-body (EPRB) model [17], [19], which introduces serial spherical joints to enable unified modeling of spatial bending and torsional responses. The EPRB model possesses a generalized expressive capacity: when the elastic modulus approaches zero, it

Z. Wu, J. Luo, S. Wei, and J. Zhang are with the school of automation, Beijing Institute of Technology, Beijing, China. (e-mail: zhiweiwu.cn@outlook.com, luojiahao.edu@outlook.com, siyiwei@bit.edu.cn).

Corresponding author: Jinhui Zhang. (e-mail: zhangjihui@bit.edu.cn).

naturally degenerates into a classical rigid-link manipulator model. Conversely, as the number of embedded magnets tends to infinity, it approximates the behavior of a magnetic continuum [22]. Based on this formulation, we conduct a well-posedness analysis of the static equilibrium equations, encompassing uniqueness, boundedness, and convergence properties. Furthermore, we derive complete analytical expressions for the Jacobian and Hessian matrices under multi-magnet configurations, thereby providing theoretical support for both kinematic analysis and controller design.

Building upon the proposed EPRB model, the second part of this paper further demonstrates its ability to facilitate geometric analysis and structural optimization of soft continuum robots. We begin by rigorously proving a key structural result: the maximum controllable degrees of freedom in a magnetically actuated soft continuum robot is exactly twice the number of embedded magnets. This finding corroborates prior empirical observations reported in many existing literature [5], [20]. Additionally, we show that when magnets are arranged axially, the EPRB model naturally reduces to the classical PRB formulation, and a closed-form solution to the equilibrium configuration can be obtained under small-angle premises. As structural optimization often aims to enhance a robot's kinematic performance, we draw inspiration from rigid manipulator design, where Jacobian-based kinematic measures (e.g., manipulability and dexterity) are widely employed to guide structural synthesis and task planning [23], [24]. We develop a differential geometry-based optimization framework around kinematic measures, which connects kinematic performances to the configuration of embedded magnets in MeSCR. Unlike rigid-link manipulators, whose structural and performance optimization can be directly formulated in joint space, soft continuum robots exhibit implicitly coupled configurations governed by elastomagnetic equilibrium. As such, optimization must be performed over the actuation or design space, with performance indices reparametrized through the configuration manifold. To resolve this, we reinterpret the equilibrium set as a smooth submanifold and apply tools from geometric measure theory to reparametrize global performance objectives over the actuation space. We derive closed-form optimal magnet configuration in representative cases and develop an efficient gradient-based numerical method for the general scenario.

Throughout the technical description, vectors and matrices are defined using lowercase and uppercase bold symbols, respectively, whereas scalars are not bolded.

II. MODELING

This section introduces the extended pseudo-rigid-body model to describe the MeSCR. Complete closed-form expressions for the manipulator Jacobian and Hessian matrices are derived. We further investigate the well-posedness of the equilibrium solution. These results provide the necessary mathematical foundation for subsequent kinematic analysis and performance optimization.

A. Forward Kinematics and Manipulator Jacobian

To meet the demands of entering narrow spaces and achieving complex deformations, MeSCRs are typically designed

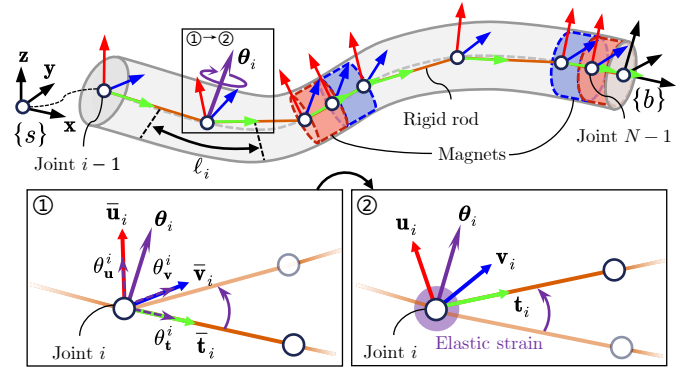


Fig. 1. Illustration of the basic concept of the EPRB model on describing the MeSCR. The continuous body is discretized by a series of rotational rigid rods with joints and frames attached. The bending and twisting deformations of the MeSCR are described by three joint variables θ_t^i , θ_u^i , and θ_v^i .

with slender structures. Certain well-founded assumptions contribute to simplifying the model [25], such as the rod remaining free of shear deformation and its cross-section always being orthogonal to the centerline. Additionally, some classical PRB models [15] neglect both twisting and stretching of the continuum. In contrast, we assume only that the continuum is inextensible, with twisting characterized by extended variables [26]. Within the EPRB model framework, a continuum robot of length L is described by a series of rigid rods. As shown in Fig. 1, N spherical joints are distributed along the centerline of the MeSCR at points of interest, connected by N rigid rods with lengths $l_i, i = 0, \dots, N-1$. We use the Voronoi region of the joint to scale the potential energies, which is defined as $\ell_i = (l_{i-1} + l_i)/2, i = 0, \dots, N-1$. An orthogonal local frame $\{\bar{\mathbf{t}}_i, \bar{\mathbf{u}}_i, \bar{\mathbf{v}}_i = \bar{\mathbf{t}}_i \times \bar{\mathbf{u}}_i\}$ is attached to each joint, with overbars indicating that the MeSCR is in a straightened reference state, and the tangent vector $\bar{\mathbf{t}}_i$ remains aligned with the direction of the successive rod. The local frame is used to determine the rotation axis for each joint, expressed as $\boldsymbol{\theta}_i = \theta_t^i \bar{\mathbf{t}}_i + \theta_u^i \bar{\mathbf{u}}_i + \theta_v^i \bar{\mathbf{v}}_i \in \mathbb{R}^3$, where $\theta_t^i, \theta_u^i, \theta_v^i \in \mathbb{R}$ are three independent joint variables. The associated rotation matrix is defined as $\mathbf{R}_i(\boldsymbol{\theta}_i) = \mathbf{e}^{[\boldsymbol{\theta}_i]_\times} \in \text{SO}(3)$, and we define a useful shorthand notation (\mathbf{R}_i^j) to represent the product of rotation matrices that $\mathbf{R}_i^j = \mathbf{R}_i \mathbf{R}_{i+1} \cdots \mathbf{R}_j$. With the notation, local frame axes in a deformed state (2), such as the tangent vector, can be easily computed by $\mathbf{t}_i = \mathbf{R}_0^i \bar{\mathbf{t}}_i$ from the reference state (1). The resulting elastic strain on the i th joint will be used to compute the elastic potential energy later.

The configuration space $(\boldsymbol{\theta})$ of the MeSCR can be written as

$$\boldsymbol{\theta} = [\boldsymbol{\theta}_0, \dots, \boldsymbol{\theta}_{N-1}]^\top \in \mathbb{T} \subset \mathbb{R}^{3N_m}. \quad (1)$$

Let a fixed base frame $\{s\}$ attach to joint 0, frame $\{b\}$ attach to the distal end, and ${}^b_b\mathbf{H} \in \text{SE}(3)$ be the associated distal pose when the MeSCR is in its zero position. The screw axes in the fixed base frame are of the form:

$$\boldsymbol{\xi}_i = \begin{bmatrix} \boldsymbol{\theta}_i \\ -\boldsymbol{\theta}_i \times \bar{\mathbf{p}}_i \end{bmatrix}$$

where $\bar{\mathbf{p}}_i$ is the reference position of the i th joint associated with l_i . Then, the forward kinematics of the MeSCR can be

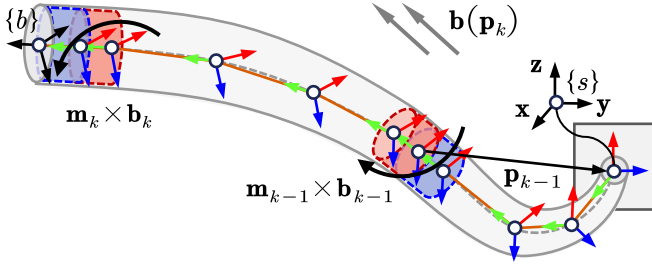


Fig. 2. Illustration of a quasi-static state of the MeSCR under an external magnetic field $\mathbf{b}(\mathbf{p}_k)$. Multiple embedded micromagnets at corresponding joints generate magnetic torques $\mathbf{m}_k \times \mathbf{b}_k$ that induce deformation in the MeSCR. When the magnetic torque and elastic moments reach the equilibrium, the MeSCR attains the quasi-static state.

represented in the following product of exponentials:

$${}^b_s\mathbf{H}(\boldsymbol{\theta}) = \mathbf{e}^{\xi_0^\wedge} \mathbf{e}^{\xi_1^\wedge} \dots \mathbf{e}^{\xi_{N-1}^\wedge} {}^b_s\bar{\mathbf{H}}(\mathbf{0}) \in \text{SE}(3).$$

We next present the analytical expression of the space Jacobian $\mathbf{J}_\theta(\boldsymbol{\theta}) \in \mathbb{R}^{6 \times 3N}$, defined in fixed frame coordinates. The space Jacobian relates small changes in joint space to distal pose as $\delta \mathbf{h} = \mathbf{J}_\theta \delta \boldsymbol{\theta}$, where $\mathbf{h} = \text{Log}({}^b_s\mathbf{H}) \in \mathbb{R}^6$ represents the distal pose in Cartesian coordinates. To facilitate calculation, the Jacobian matrix is partitioned into blocks, with each block corresponding to a joint space group as

$$\mathbf{J}_\theta^s = \left[\frac{\partial \mathbf{h}}{\partial \theta_0}, \frac{\partial \mathbf{h}}{\partial \theta_1}, \dots, \frac{\partial \mathbf{h}}{\partial \theta_{N-1}} \right] \quad (2)$$

where the derivative with respect to θ_i is given by

$$\frac{\partial \mathbf{h}}{\partial \theta_i} = \text{Ad}_{\mathbf{e}^{\xi_0^\wedge} \dots \mathbf{e}^{\xi_{i-1}^\wedge}} \mathbf{J}_{\mathbf{H}_i}^{\xi_i} \frac{\partial \xi_i}{\partial \theta_i} \in \mathbb{R}^{6 \times 3}$$

with $\frac{\partial \xi_i}{\partial \theta_i} = [\mathbf{I}_3, -[\bar{\mathbf{p}}_i]_\times]^\top$, and $\mathbf{J}_{\mathbf{H}_i}^{\xi_i}$ is the left Jacobian of the SE(3) manifold, as discussed in [27]. To conclude, we note the following relationship between the space Jacobian and the body Jacobian ($\mathbf{J}_\theta^b(\boldsymbol{\theta})$) in case of need:

$$\mathbf{J}_\theta^b = \text{Ad}_{\mathbf{e}^{\xi_0^\wedge} \dots \mathbf{e}^{\xi_{N-1}^\wedge}}^{-1} \mathbf{J}_\theta^s. \quad (3)$$

Also for brevity, \mathbf{J}_θ will be referred to \mathbf{J}_θ^s unless specified.

B. Equations of Motion

The MeSCR's equations of motion are derived from the Lagrangian mechanics, which are formulated based on the MeSCR's potential energy. As shown in Fig. 2, the MeSCR is allowed to bend, twist, and magnetic actuable. Thus, the total potential energy features elastic strains and magnetic moments, which are decomposed into the elastic (\mathcal{E}_e) and magnetic (\mathcal{E}_m) potential energies as

$$\mathcal{E} = \mathcal{E}_e + \mathcal{E}_m. \quad (4)$$

The respective energies are formulated as follows.

1) *Elastic Potential Energy*: In general deformation conditions, the elastic strain can be approximated as a linear function of the joint angle θ_i , [15], [26], [28]. The quadratic form of the elastic strain formulates the elastic potential energy as

$$\begin{aligned} \mathcal{E}_e &= \frac{1}{2} \sum_{i=0}^{N-1} (\theta_i - \bar{\theta}_i)^\top \Lambda_i (\theta_i - \bar{\theta}_i) \\ &= \frac{1}{2} (\boldsymbol{\theta} - \bar{\boldsymbol{\theta}})^\top \Lambda (\boldsymbol{\theta} - \bar{\boldsymbol{\theta}}) \end{aligned}$$

where $\Lambda_i = \text{diag}(\frac{2G_i I_i}{\ell_i}, \frac{E_i I_i}{\ell_i}, \frac{E_i I_i}{\ell_i})$, G_i , E_i , I_i are the shear modulus, Young's modulus, and cross-sectional inertia of the i th joint, respectively. The block-diagonal matrix Λ is composed of Λ_i , referred to as the joint stiffness matrix. We also note $G_i = \frac{E_i}{2(1+\rho_i)}$ for the isotropic material used in the MeSCR, where ρ_i represents the Poisson's ratio. The material properties of each joint are determined by whether it comprises a hard-magnetic material or a soft matrix, both of which exhibit a positive Poisson's ratio.

2) *Magnetic Potential Energy*: As shown in Fig. 2, each embedded micromagnet is treated as an independent joint, with additional joints added on either side to assist the description. The joint indices of all N_m micromagnets constitute an index set $\mathbb{K} \subset \mathbb{Z}$. Given that the robot operates under a constant temperature, the formulation aligns with the standard Helmholtz free energy without thermal variations [10]. Additional terms with thermal effects can be found in [29]. In this case, the magnetic potential energy of the MeSCR is given by

$$\mathcal{E}_m = - \sum_{k \in \mathbb{K}} \mathbf{m}_k^\top \mathbf{b}(\mathbf{p}_k)$$

where $\mathbf{m}_k = \mathbf{R}_0^k \bar{\mathbf{m}}_k \in \mathbb{R}^3$ is the magnetic dipole moments of the k th magnet with modulus $M_k = \|\bar{\mathbf{m}}_k\|$ and $\mathbf{b}(\mathbf{p}_k) \in \mathbb{R}^3$ denote the external magnetic field with modulus $B_k = \|\mathbf{b}(\mathbf{p}_k)\|$. For readability, we sometimes denote $\mathbf{b}(\mathbf{p}_k)$ in \mathbf{b}_{k_i} , in which $i = 0, 1, \dots, N_m - 1$.

It is worth noting that some operational scenarios of MeSCR (e.g., interaction with human tissue) typically require low-speed motion to ensure operational safety. Therefore, it is generally assumed that MeSCR operates in quasi-static states, where the inertia terms can be neglected. The dynamic analysis of MeSCR is thus reduced to finding the equilibrium between internal/external forces and potential energy, which can be obtained by solving the following simplified Lagrangian equation:

$$\nabla_{\boldsymbol{\theta}} \mathcal{E}_e + \nabla_{\boldsymbol{\theta}} \mathcal{E}_m + \boldsymbol{\tau}(\boldsymbol{\theta}) = \mathbf{0} \quad (5)$$

where $\boldsymbol{\tau}(\boldsymbol{\theta})$ is the internal/external applied torques that can be considered (e.g., gravity torques). We further provide the analytical expressions for the gradients and Hessians of the potential energies, which can improve the accuracy and efficiency of calculations. The gradient and Hessian of \mathcal{E}_e are

straightforward, whereas we focus on computing that of \mathcal{E}_m .

$$\begin{aligned} \nabla_{\theta_i} \mathcal{E}_m &= - \sum_{k \in \mathbb{K}, k \geq i} \left([\mathbf{m}_k]^\top \times \mathbf{R}_0^\top \mathbf{J}_{\mathbf{R}_r}^{\theta_i} \right)^\top \mathbf{b}(\mathbf{p}_k) \\ &\quad - \sum_{k \in \mathbb{K}, k \geq i} \left(\frac{\partial \mathbf{b}(\mathbf{p}_k)}{\partial \mathbf{p}_k} \frac{\partial \mathbf{p}_k}{\partial \theta_i} \right)^\top \mathbf{m}_k \\ &\triangleq \underbrace{-\mathbf{M}_i(\boldsymbol{\theta}) \mathbf{b}}_{\text{magnetic torques}} - \sum_{k \in \mathbb{K}, k \geq i} \left(\frac{\partial \mathbf{p}_k}{\partial \theta_i} \right)^\top \underbrace{(\nabla_{\mathbf{p}_k} \mathbf{b}) \mathbf{m}_k}_{\text{magnetic forces}} \end{aligned} \quad (6)$$

where $\mathbf{J}_{\mathbf{R}_r}^{\theta_i}$ represents the right Jacobian of SO(3) manifold associated with θ_i [30]. We reorganize the expression by grouping the multiplicative terms into matrix $\mathbf{M}_i(\boldsymbol{\theta}) \in \mathbb{R}^{3 \times 3N_m}$ and introducing vector $\mathbf{b} = [\mathbf{b}_{k_0}^\top, \dots, \mathbf{b}_{k_{N_m-1}}^\top]^\top \in \mathbb{B} \subset \mathbb{R}^{3N_m}$ to obtain a compact form. For precise calculations, $\frac{\partial \mathbf{p}_k}{\partial \theta_i}$ can be derived from (3). However, the magnetic force is usually negligible in comparison to the magnetic torques, which implies the following explicit representation of (5) as

$$\boldsymbol{\Lambda}(\boldsymbol{\theta} - \bar{\boldsymbol{\theta}}) + \boldsymbol{\tau}(\boldsymbol{\theta}) = \mathbf{M}(\boldsymbol{\theta}) \mathbf{b} \quad (7)$$

where $\mathbf{M}(\boldsymbol{\theta}) = [\mathbf{M}_0^\top, \dots, \mathbf{M}_{N-1}^\top]^\top \in \mathbb{R}^{3N \times 3N_m}$. By developing (7) and performing some rearrangements, the joint space compliance relation between the variation of the actuating magnetic field ($\delta \mathbf{b}$) and the configuration variation ($\delta \boldsymbol{\theta}$) is obtained:

$$\underbrace{\left(\boldsymbol{\Lambda} + \frac{\partial^2 \mathcal{E}_m}{\partial \boldsymbol{\theta} \partial \boldsymbol{\theta}^\top} + \frac{\partial \boldsymbol{\tau}}{\partial \boldsymbol{\theta}} \right)}_{\triangleq \mathbf{S}} \delta \boldsymbol{\theta} = \mathbf{M}(\boldsymbol{\theta}) \delta \mathbf{b}$$

where the Hessian of \mathcal{E}_m (denoted in \mathbf{S}_m) is given in the supplementary material and $\mathbf{S} \in \mathbb{R}^{3N \times 3N}$ denotes the Hessian matrix of stiffness. Hence, the joint-space compliance relation reads

$$\delta \boldsymbol{\theta} = \mathbf{S}^{-1} \mathbf{M}(\boldsymbol{\theta}) \delta \mathbf{b}. \quad (8)$$

Premultiplying (8) by the space Jacobian (2) yields the Cartesian compliance mapping from magnetic field perturbations to distal pose variations:

$$\delta \mathbf{h} = \mathbf{J}_\theta \mathbf{S}^{-1} \mathbf{M}(\boldsymbol{\theta}) \delta \mathbf{b} \triangleq \mathbf{J}_b \delta \mathbf{b} \quad (9)$$

where $\mathbf{J}_b \in \mathbb{R}^{6 \times 3N_m}$ is referred to as the actuation Jacobian. We close this subsection by introducing two useful propositions:

Proposition 1. *The matrix-valued function $\mathbf{M}(\boldsymbol{\theta})$ and the magnetic torque $\mathbf{M}(\boldsymbol{\theta}) \mathbf{b}$ are bounded on \mathbb{R}^{3N} with positive constants \mathcal{M}_0 and \mathcal{M} such that $\|\mathbf{M}(\boldsymbol{\theta})\| \leq \mathcal{M}_0$ and $\|\mathbf{M}(\boldsymbol{\theta}) \mathbf{b}\| \leq \mathcal{M}$ for all $\boldsymbol{\theta} \in \mathbb{R}^{3N}$, respectively.*

Proposition 2. *The vector-valued function $\mathbf{M}(\boldsymbol{\theta}) \mathbf{b}$ is Lipschitz continuous on \mathbb{R}^{3N} with a Lipschitz constant \mathcal{L} such that $\|\mathbf{M}(\boldsymbol{\theta}) \mathbf{b} - \mathbf{M}(\boldsymbol{\varphi}) \mathbf{b}\| \leq \mathcal{L} \|\boldsymbol{\theta} - \boldsymbol{\varphi}\|$ for all $\boldsymbol{\theta}, \boldsymbol{\varphi} \in \mathbb{R}^{3N}$.*

Proof. The proofs are deferred to Appendix A. ■

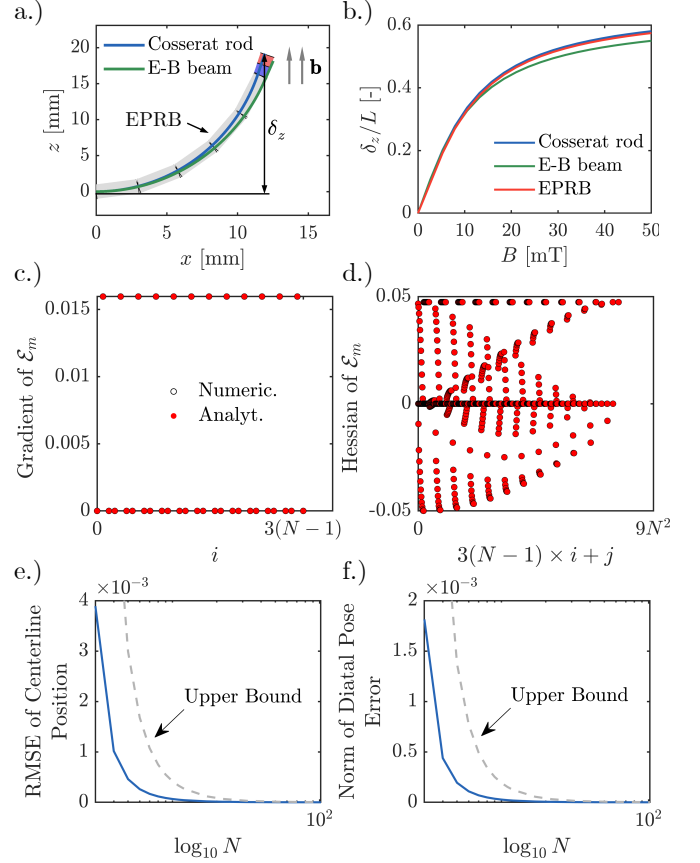


Fig. 3. a.) Comparison of the predicted deformed shapes of the MeSCR with an embedded magnet at the distal end, under external magnetic fields, using the Cosserat rod, Euler-Bernoulli beam, and EPRB models. b.) The normalized deflection (δ_z/L) obtained from the three models is plotted against the magnetic field strength (B [mT]). c.) Comparison of the gradients, and d.) Hessians of \mathcal{E}_m , both analytical and numerical results. The indices i and j range from 0 to $3(N-1)$. e.) The root-mean-square-error (RMSE) of the centerline position, and d.) the norm of distal pose error plotted against the number of joints.

TABLE I
GEOMETRIC AND MATERIAL PROPERTIES OF THE MESCR#1

Parameters (Description)	Value [Unit]
N (Number of joints)	7 [-]
L_f (Length of the flexible rod)	30 [mm]
L_m (Length of the magnet)	3 [mm]
I (Area moment of inertia)	0.7854 [mm ⁴]
E_f (Young's modulus of the flexible rod)	5 [MPa]
E_m (Young's modulus of the magnet)	160 [GPa]
M (Modulus of the magnetic dipole moment)	10^{-2} [A · m ²]

C. Analysis and Validation of Equilibrium Solution

We first analyze the equilibrium solution. Assuming the robot to be naturally straight ($\bar{\boldsymbol{\theta}} = \mathbf{0}$), and $\boldsymbol{\tau}(\boldsymbol{\theta})$ is ruled out. Then, reformulate (7) derives the following fixed-point equation:

$$\boldsymbol{\theta} = \boldsymbol{\Lambda}^{-1} \mathbf{M}(\boldsymbol{\theta}) \mathbf{b}. \quad (10)$$

Observe that the right-hand side of the equation represents a continuous mapping with respect to $\boldsymbol{\theta}$. We present the following theorem regarding the uniqueness of the solution.

Theorem 1. *There exists a unique equilibrium solution to (10) if the following inequality holds:*

$$\max_{k \in \mathbb{K}} B_k < \frac{\pi}{4} \frac{\lambda_{\min}(\mathbf{\Lambda})}{\sum_{k \in \mathbb{K}} k M_k} \quad (11)$$

where $\lambda_{\min}(\cdot)$ denotes the smallest eigenvalue of a matrix.

Proof. Based on the Proposition 2, the Lipschitz constant of the continuous mapping can be estimated by

$$\left\| \mathbf{\Lambda}^{-1} \frac{\partial}{\partial \boldsymbol{\theta}} \mathbf{M}(\boldsymbol{\theta}) \mathbf{b} \right\| = \|\mathbf{\Lambda}^{-1} \mathbf{S}_m\| \leq \|\mathbf{\Lambda}^{-1}\| \mathcal{L} = \lambda_{\min}^{-1}(\mathbf{\Lambda}) \mathcal{L}.$$

From (11), it follows that $\lambda_{\min}^{-1}(\mathbf{\Lambda}) \mathcal{L} < 1$. Then, $\mathbf{\Lambda}^{-1} \mathbf{M}(\boldsymbol{\theta}) \mathbf{b}$ is a contraction mapping on \mathbb{R}^{3N} . By Banach's fixed-point theorem, there exists a unique equilibrium point to (10). ■

The inequality provides a sufficient condition to guarantee the uniqueness of a globally attractive equilibrium point for any initial condition. Notably, the upper bound is solely determined by the material properties: E , I , L , M_k , and is independent of the joint number N (note that $N \bar{\ell}_i \approx L$). The limitation on the external magnetic field strength can be explained by the critical buckling instability of the magneto-elastic material [31]. We found it intriguing that when each joint is magnetized, the resulting upper bound exhibits a striking structural resemblance to that derived in our previous work [32] on magnetic continua, differing only slightly in the coefficients. This similarity highlights the underlying consistency in the physical principles governing continuum and discreteness. Furthermore, Theorem 1 also ensures \mathbf{S} to be invertible. By applying Weyl's inequality, one can easily verify that $\lambda_{\min}(\mathbf{S}) \geq \lambda_{\min}(\mathbf{\Lambda}) - \mathcal{L} > 0$.

Although the upper bound remains a conservative estimate, once the external magnetic field strength exceeds this upper limit, (10) may admit multiple equilibria pertaining to different initial conditions [21]. Therefore, selecting appropriate initial values for the iteration becomes crucial to ensuring convergence and avoiding undesirable behaviors. The solution trajectory can be described by the constructed dynamic system $\frac{d\boldsymbol{\theta}}{dt} = -\frac{\partial \mathcal{E}}{\partial \boldsymbol{\theta}}$ with initial condition $\boldsymbol{\theta}(0)$, which can also be regarded as a gradient flow that minimizes the energy function $\mathcal{E}(\boldsymbol{\theta})$. We propose the following theorem and lemmas, which guarantee that the solution is bounded and convergent by choosing an appropriate initial condition.

Lemma 1. *For any initial condition $\boldsymbol{\theta}(0)$, the solution trajectory $\boldsymbol{\theta}(t)$ is bounded that*

$$\|\boldsymbol{\theta}(t)\| \leq \max \left\{ \|\boldsymbol{\theta}(0)\|, \frac{\mathcal{M}}{\lambda_{\min}(\mathbf{\Lambda})} \right\}.$$

Proof. Consider the Lyapunov function $V(\boldsymbol{\theta}) = \frac{1}{2} \|\boldsymbol{\theta}\|^2$, the derivative of $V(\boldsymbol{\theta})$ with respect to time is $\dot{V}(\boldsymbol{\theta}) = \boldsymbol{\theta}^\top (-\mathbf{\Lambda} \boldsymbol{\theta} + \mathbf{M}(\boldsymbol{\theta}) \mathbf{b}) = -\boldsymbol{\theta}^\top \mathbf{\Lambda} \boldsymbol{\theta} + \boldsymbol{\theta}^\top \mathbf{M}(\boldsymbol{\theta}) \mathbf{b}$. Using Proposition 1, the upper bound of $\dot{V}(\boldsymbol{\theta})$ is derived as $\dot{V}(\boldsymbol{\theta}) \leq -\lambda_{\min}(\mathbf{\Lambda}) \|\boldsymbol{\theta}\|^2 + \mathcal{M} \|\boldsymbol{\theta}\|$. Let $W(t) = \sqrt{2V(\boldsymbol{\theta})} = \|\boldsymbol{\theta}\|$, one can find out that: $\dot{W}(t) = \frac{\dot{V}(\boldsymbol{\theta})}{W(t)} \leq -\lambda_{\min} W(t) + \mathcal{M}$. Applying Grönwall's inequality, we obtain $W(t) \leq W(0) e^{-\lambda_{\min}(\mathbf{\Lambda}) t} + \frac{\mathcal{M}}{\lambda_{\min}(\mathbf{\Lambda})} (1 - e^{-\lambda_{\min}(\mathbf{\Lambda}) t})$. Observed that as $t \rightarrow \infty$, the exponential term vanishes, leading to $\lim_{t \rightarrow \infty} W(t) \leq \frac{\mathcal{M}}{\lambda_{\min}(\mathbf{\Lambda})}$.

This completes the proof, establishing that $\|\boldsymbol{\theta}(t)\|$ remains $\|\boldsymbol{\theta}(t)\| \leq \max \left\{ \|\boldsymbol{\theta}(0)\|, \frac{\mathcal{M}}{\lambda_{\min}(\mathbf{\Lambda})} \right\}$. ■

Lemma 2. *Let $\boldsymbol{\theta}^*$ be any equilibrium point of (10). Using Proposition 1, we have $\|\boldsymbol{\theta}^*\| = \|\mathbf{\Lambda}^{-1} \mathbf{M}(\boldsymbol{\theta}^*) \mathbf{b}\| \leq \frac{\mathcal{M}}{\lambda_{\min}(\mathbf{\Lambda})}$.*

Theorem 2. *The solution trajectory $(\boldsymbol{\theta}(t))$ will always converge to the largest invariant subset of the equilibrium point set if the initial condition satisfies $\|\boldsymbol{\theta}(0)\| \leq \frac{\mathcal{M}}{\lambda_{\min}(\mathbf{\Lambda})}$.*

Proof. Choose the Lyapunov function $V(\boldsymbol{\theta}) = \mathcal{E}(\boldsymbol{\theta})$, whose derivative along the solution trajectory satisfies $\dot{V}(\boldsymbol{\theta}) = -\|\frac{\partial \mathcal{E}}{\partial \boldsymbol{\theta}}\|^2 \leq 0$, with equality holding if and only if $\boldsymbol{\theta}$ is an equilibrium point. Consider the positively invariant set $\Omega = \left\{ \boldsymbol{\theta} \in \mathbb{R}^{3N} \mid \|\boldsymbol{\theta}\| \leq \frac{\mathcal{M}}{\lambda_{\min}(\mathbf{\Lambda})} \right\}$ (Lemma 1), which contains all equilibrium points (Lemma 2). By Brouwer's fixed-point theorem, there exists at least one equilibrium point within Ω , that is, $\dot{V}(\boldsymbol{\theta}) \leq 0$ holds for all $\boldsymbol{\theta} \in \Omega$. According to LaSalle's invariance principle, every trajectory within Ω converges to the largest invariant subset where $\dot{V}(\boldsymbol{\theta}) = 0$. ■

When the external magnetic field changes, requiring the recalculation of the equilibrium point, Theorem 2 provides a natural choice for the initial condition as $\boldsymbol{\theta}(0) = \mathbf{0}$ because $\forall \mathbf{b} \in \mathbb{B}, \mathcal{M} \geq 0$. One can also choose the nearby solution as an initial guess if \mathbf{b} continuously increases. For small perturbations on \mathbf{b} , the corresponding $\delta \boldsymbol{\theta}$ can be calculated by (8). Moreover, from Proposition 1 and the fact that $\boldsymbol{\theta} = \mathbf{0}$ is the unique equilibrium solution when $\mathbf{b} = \mathbf{0}$, we deduce that $\frac{\partial \mathcal{E}}{\partial \boldsymbol{\theta}}$ is Lipschitz continuous with respect to \mathbf{b} , and the equilibrium points depends continuously on it.

We then consider the commonly used magnetic continuum (MeSCR#1), featuring an embedded magnet at the distal end. In the example shown in Fig. 3a, the geometric and material properties are listed in Tab. I. By solving (5) using gradient methods and $\boldsymbol{\theta}(0) = \mathbf{0}$ as the initial condition, we compare the shapes of MeSCR under a uniform magnetic field between the EPRB model and two continuous models (Cosserat rod [13] and Euler-Bernoulli beam [33]). The normalized deflection (δ_z/L) is plotted against the magnetic field strength B [mT], ranging from 0 to 50, as shown in Fig. 3b. The results indicate that the EPRB model aligns well with continuous models in predicting deformation and deflection. Moreover, the analytical and numerical results for the gradients and Hessians of \mathcal{E}_m are compared in Fig. 3c and Fig. 3d with the indices i and j range from 0 to $3(N-1)$. The close agreement between the computations validates the correctness of the analytical derivation and contributes to improving the computational efficiency and stability of \mathbf{J}_b .

Notably, using fewer joints does not introduce significant truncation errors and offers a computational speed advantage over BVP-solving models. Fig. 3e and Fig. 3f show the root-mean-square error (RMSE) of the centerline position and the distal pose error norm as the joint count increases from 3 to 100, benchmarked against 200 joints. Results demonstrate that RMSE decreases proportionally to $1/N^2$, with an error bound established in our previous work [34]. Using 7 joints achieves an RMSE below the acceptable 10^{-4} threshold. Additionally, the distal pose error norm declines rapidly as N grows,

confirming that fewer joints can accurately compute the distal pose under external magnetic fields. This analysis leads to a key insight: the performance index of the actuation Jacobian is largely insensitive to N and can be understood as an inherent property of the robot in a specific configuration.

III. ENHANCING KINEMATIC PERFORMANCES

This section focuses on the structural optimization of Me-SCRs to enhance kinematic performances, including manipulability and dexterity. Prior to the optimization, we perform some kinematic analysis of the actuation Jacobian, uncovering how different magnet configuration shape the robot's controllable DoF achievable workspace.

A. Kinematics Analysis

We define the controllable degrees of freedom (DoF) as the independently actuated direction of the task-space twist, which corresponds to the row rank of the actuation Jacobian (\mathbf{J}_b). The following theorem reveals the relation between it and the configuration of embedded magnets:

Theorem 3. *The controllable DoF of the MeSCR does not exceed twice the number of embedded magnets.*

Proof. Recall that the actuation Jacobian $\mathbf{J}_b = \mathbf{J}_\theta \mathbf{S}^{-1} \mathbf{M}(\theta)$, the post-multiplied matrix ($\mathbf{M}(\theta)$) can be rewritten as

$$\mathbf{M}(\theta) = \mathbf{D}_{kN_m-1}^\top \left(\begin{bmatrix} \mathbf{1}_{k_0} & \dots & \mathbf{1}_{k_{N_m-1}} \\ \mathbf{0}_{N-k_0} & & \mathbf{0}_{N-k_{N_m-1}} \end{bmatrix} \otimes \mathbf{I}_{3 \times 3} \right) \times \text{blkdiag} \left\{ [\mathbf{m}_{k_0}]_\times, \dots, [\mathbf{m}_{k_{N_m-1}}]_\times \right\} \quad (12)$$

in which the block diagonal matrix \mathbf{D}_{kN_m-1} is provided in (24) and $\mathbf{1}_k$ denotes the all-ones vector of k dimensions. To determine the rank of $\mathbf{M}(\theta)$, one starts by noting that

$$\text{rk} \left(\begin{bmatrix} \mathbf{1}_{k_0} & \dots & \mathbf{1}_{k_{N_m-1}} \\ \mathbf{0}_{N-k_0} & & \mathbf{0}_{N-k_{N_m-1}} \end{bmatrix} \otimes \mathbf{I}_3 \right) = 3N_m.$$

Applying Sylvester's rk inequality, we obtain:

$$\text{rk}(\mathbf{M}(\theta)) \leq \min \left\{ \sum_{i=0}^{N_m-1} \text{rk} \left(\mathbf{R}_0^{k_i} \mathbf{J}_{\mathbf{R}_r}^{\theta_{k_i}} \right), \sum_{i=0}^{N_m-1} \text{rk}([\mathbf{m}_{k_i}]_\times) \right\} = 2N_m, \quad (13)$$

and

$$\text{rk}(\mathbf{M}(\theta)) \geq \sum_{i=0}^{N_m-1} \left(\text{rk} \left(\mathbf{R}_0^{k_i} \mathbf{J}_{\mathbf{R}_r}^{\theta_{k_i}} \right) + \text{rk}([\mathbf{m}_{k_i}]_\times) \right) - 3N_m = 2N_m. \quad (14)$$

Here we used the facts that $\mathbf{J}_{\mathbf{R}_r}^{\theta_{k_i}}$ and $\mathbf{R}_0^{k_i}$ are both invertible and the rank of a skew-symmetric matrix remains 2. Combined (13) with (14) leads to the following result:

$$\text{rk}(\mathbf{M}(\theta)) = 2N_m.$$

Consequently, an important conclusion is derived as $\text{rk}(\mathbf{J}_b) \leq \min \{6, \text{rk}(\mathbf{M}(\theta))\} = \min \{6, 2N_m\}$. ■

We proceed with a brief discussion on MeSCR's structural configuration with different N_m :

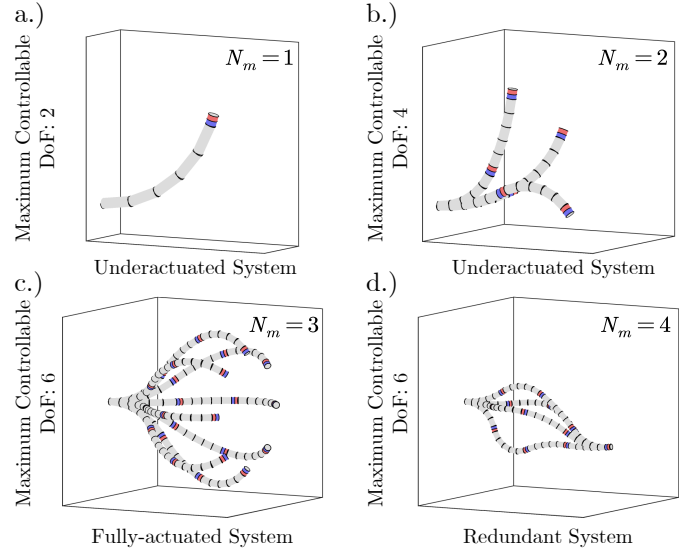


Fig. 4. Deformation of the MeSCR with different numbers of embedded magnets ($N_m = 1, 2, 3, 4$), corresponding to subfigures a.), b.), c.), and d.). As N_m increases, the MeSCR is characterized as underactuated for $N_m = 1, 2$, fully-actuated for $N_m = 3$, and redundant for $N_m = 4$.

- $N_m = 1$ [2]–[4] (see Fig. 4a.): The simplest yet most used configuration. The single magnet is typically embedded at the distal end to maximize torque transmission. From Theorem 3, we show that at most 2 DoF of the task-space twist is controllable, which is consistent with the conclusion in [18].
- $N_m = 2$ [19], [20], [35], [36] (see Fig. 4b.): Multimodality properties emerged since the orientation of embedded magnets is designable. However, at most 4 DoF are controllable, which still characterizes the system as **underactuated**.
- $N_m = 3$ [13], [37], [38] (see Fig. 4c.): The structural configuration of the embedded magnets is also optimizable. The maximum controllable DoF is 6, indicating that the MeSCR is **fully-actuated**.
- $N_m \geq 4$ [39]–[41] (see Fig. 4d.): Adopted by many commercial products. The column rank of \mathbf{J}_b exceeds its row rank, indicating that the MeSCR is a **redundant** system and the number of redundant DoF is $2N_m - 6$.

The maximum controllable DoF will also be limited by the actuating field. As N_m increases, achieving fully-actuated or redundant control requires each embedded magnet to be paired with an independent actuating field. However, generating independently controllable actuating fields at arbitrary positions within the workspace is highly challenging. While some advanced equipment may be capable of this [42], it is not feasible for most conventional systems. For example, when the actuating field is spatially uniform within the workspace, which can be expressed as $\mathbf{b} = \mathbf{U}_u \mathbf{b}_u$ with $\mathbf{U}_u = \mathbf{1}_{N_m} \otimes \mathbf{I}_3$ and $\mathbf{b}_u \in \mathbb{R}^3$. In this case, the maximum controllable DoF will not exceed 3. To reduce the number of design variables, we assume all embedded magnets have uniform material and geometric properties, which also facilitates the manufacturing process. Consequently, the orientation and position of the em-

bedded magnets become the primary variables to be optimized.

In existing commercial products, embedded magnets are generally placed along the catheter's axial direction. For N_m magnets, this arrangement leads to 2^{N_m} possible permutations. However, if the actuating magnetic field of each magnet is independently controllable, the directions of the magnetic moments become redundant. This redundancy arises because of the relationship: $[\pm \mathbf{m}_k]_{\times} \mathbf{b}_k = [\mathbf{m}_k]_{\times} (\pm \mathbf{b}_k)$, indicating that the effect of flipping a magnetic moment's direction can always be compensated by reversing the corresponding magnetic field direction. Based on this reasoning, we assume that the magnetic field can only undergo an overall direction reversal. For systems driven by electromagnets, this can be easily achieved by altering the current direction.

Aligning the magnetic moments along the axial direction significantly reduces the optimization search space but imposes a limitation on the motion of the MeSCR. Specifically, this arrangement restricts the MeSCR to *material-twist-free* due to the decoupling of twisting and bending, as ensured by the isotropic and axially symmetric properties of its soft matrix.

Theorem 4 (Material-twist-free). *The MeSCR is material-twist-free ($\boldsymbol{\theta}_i^{\top} \bar{\mathbf{t}}_i = 0$) for any actuating magnetic field, provided that the embedded magnets' magnetic moments are aligned axially, i.e., $\bar{\mathbf{m}}_k = \pm M_k \bar{\mathbf{t}}$, and the magnetic field strength satisfies:*

$$\max_{k \in \mathbb{K}} B_k \leq \frac{\sqrt{6} \lambda_{\min}(\boldsymbol{\Lambda})}{\sum_{k \in \mathbb{K}} M_k}. \quad (15)$$

Proof. The proof is detailed in the supplementary material. ■

Noticing that $\frac{\sqrt{6} \lambda_{\min}(\boldsymbol{\Lambda})}{\sum_{k \in \mathbb{K}} M_k} \propto N^2$, as $N \rightarrow \infty$, Theorem 4 holds for any actuating magnetic field. This upper bound characterizes the ability of the discrete model with N joints to approximate the continuum, as discussed in Section II-C. We found an alternative form of the equilibrium equation (10) from the underlying proof:

$$\boldsymbol{\theta}_i^* = \frac{\sum_{k \geq i} \mathbf{v}_k}{\lambda_{\max}(\boldsymbol{\Lambda}_i)} = \frac{\sum_{k \geq i} [\mathbf{R}_0^{k\top}(\boldsymbol{\theta}^*) \mathbf{b}_k]_{\times}^{\top} \bar{\mathbf{m}}_k}{\lambda_{\max}(\boldsymbol{\Lambda}_i)}. \quad (16)$$

For any initial condition satisfying the assumptions of Theorem 2, the associated equilibrium state is guaranteed to exhibit zero torsional components. The configuration space (1) thus can be degenerated to a simplified model as presented in [16]. Moreover, the joint stiffness matrix reduces to $\boldsymbol{\Lambda}_i = \Lambda_i \mathbf{I}_3$ with $\Lambda_i = \frac{E_i I_i}{\ell_i}$, and we denote $\lambda_{\min}(\boldsymbol{\Lambda}) = \Lambda_{\min}$. We emphasize its distinction from geometric-twist-free, which requires $\boldsymbol{\theta}_i^{\top} \bar{\mathbf{t}}_i = 0$. It should be known that geometric torsion may still exist under the material-twist-free condition. However, if the external magnetic field is coplanar, the following corollary holds:

Corollary 1. *Define the plane $\Pi = \text{span}\{\bar{\mathbf{t}}, \mathbf{v}\} \subset \mathbb{R}^3$, where $\mathbf{v} \in \mathbb{R}^3$ is linearly independent of $\bar{\mathbf{t}}$. Suppose $\forall k \in \mathbb{K}$, $\bar{\mathbf{m}}_k = \pm M_k \bar{\mathbf{t}}$ and $\mathbf{b}_k \in \Pi$. Then there exists an equilibrium configuration $\boldsymbol{\theta}^* \in \mathbb{R}^{3N}$ such that the centerline of the MeSCR lies entirely within the plane Π .*

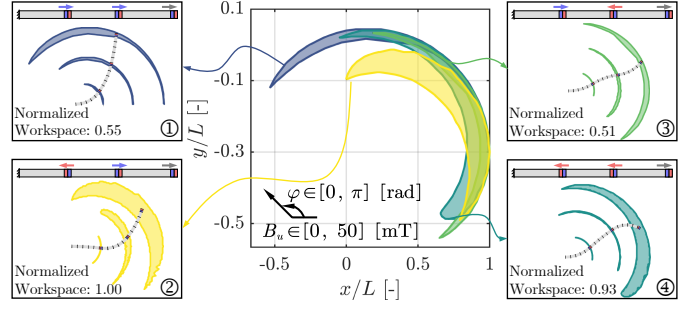


Fig. 5. Comparison of the half-planar normalized workspace of MeSCRs with equidistant placement of three embedded magnets.

Proof. The proof is constructive. Let $\boldsymbol{\theta}_i^* = \theta_i^* \mathbf{n}$, where $\mathbf{n} = \frac{\bar{\mathbf{t}} \times \mathbf{v}}{\|\bar{\mathbf{t}} \times \mathbf{v}\|}$ is the unit vector orthogonal to Π . Since $\mathbf{b}_k \in \Pi$, we notice that $\mathbf{R}_0^{k\top}(\boldsymbol{\theta}^*) \mathbf{b}_k = \mathbf{R}(-\sum_i \theta_i^* \mathbf{n}) \mathbf{b}_k \in \Pi$. Then $\forall k \in \mathbb{K}$, $[\bar{\mathbf{m}}_k]_{\times} \mathbf{R}_0^{k\top} \mathbf{b}_k \in \text{span}\{\mathbf{n}\}$. Hence $\boldsymbol{\theta}_i^* = \theta_i^* \mathbf{n}$ is a solution to (16). The corresponding tangent vectors $\bar{\mathbf{t}}_i = \mathbf{R}_0^i \bar{\mathbf{t}}_i \in \Pi$, thus the centerline lies entirely within the plane Π . ■

Specially, if the initial value is chosen as $\boldsymbol{\theta}(0) = \mathbf{0}$, then the gradient-based iteration evolves within the subspace $\text{span}\{\mathbf{n}\}$. By Theorem 2, the optimization trajectory will converge to a planar equilibrium configuration satisfying $\boldsymbol{\theta}_i = \theta_i \mathbf{n}$. We can further derive a closed-form expression under the small-angle premise, wherein the cumulative rotation matrix admits the first-order expansion: $\mathbf{R}(\sum_{i=0}^k \theta_i \mathbf{n}) \approx \mathbf{I}_3 + \sum_{i=0}^k \theta_i [\mathbf{n}]_{\times}$. Substituting this into the total potential energy yields

$$\mathcal{E} \approx \sum_{i=0}^{N-1} \frac{1}{2} \Lambda_i \theta_i^2 + \sum_{i=0}^{N-1} \theta_i \left(\sum_{k \in \mathbb{K}, k \geq i} \bar{\mathbf{m}}_k^{\top} [\mathbf{n}]_{\times} \mathbf{b}_k \right) - \sum_k \bar{\mathbf{m}}_k^{\top} \mathbf{b}_k.$$

The optimization problem $\min_{\boldsymbol{\theta}} \mathcal{E}$ thus has the explicit solution

$$\theta_i = \frac{1}{\Lambda_i} \sum_{k \in \mathbb{K}, k \geq i} \bar{\mathbf{m}}_k^{\top} [\mathbf{b}_k]_{\times} \mathbf{n}. \quad (17)$$

It can be verified that this also corresponds to the general solution of (16) under the small-angle premise.

B. Optimization Methodology

The position and orientation of embedded magnets determine the magnetic response deformation of MeSCRs under the same magnetic field. For instance, embedded magnets with variable positions have been employed to expand the MeSCR's workspace [8]. In the PRB model, the length of embedded magnets can be defined by the Voronoi length as $L_k \triangleq \sum_{i \leq k} \ell_i, \forall k \in \mathbb{K}$. From (10), it follows that the flexible segment beyond the last embedded magnet is unactuated. Consequently, it does not affect the workspace volume of the MeSCR, nor any performance metric defined using a left-invariant Riemannian metric. Therefore, one of the magnets is fixed at the distal end of the continuum ($L_{k_{N_m-1}} = L$), leaving $N_m - 1$ decision variables. Additionally, let the flexible segments between adjacent magnets be uniformly distributed and have appropriate spacing to mitigate magnetic coupling effects. Based on the previous assumption regarding the overall

reversal of the magnetic field direction, any configuration of axially placed magnets has a corresponding symmetrical configuration, resulting in a total of 2^{N_m-1} possible combinations.

Expanding the workspace volume is a key objective in the optimal design of MeSCRs [43]. However, comparing workspace volumes across MeSCRs with different embedded magnet orientations is of limited significance, unless the focus is explicitly on spatial coverage by the distal end. As shown in Fig. 5, we compared the normalized half-workspace areas of the four MeSCRs under equidistant configurations. The results indicate that ② achieves the largest normalized workspace area, whereas ③ has the smallest. Nevertheless, despite its smaller workspace area, ① may still reach regions that are inaccessible to ②. Therefore, our focus shifts to the global indices of MeSCRs with fixed magnet orientations within their respective workspaces.

Recall that ${}^b_s\mathbf{H}(\boldsymbol{\theta}) : \mathbb{T} \rightarrow \text{SE}(3)$ is the forward kinematic map of the MeSCR. Let $z({}^b_s\mathbf{H}(\boldsymbol{\theta}); L_k) : \mathbb{T} \rightarrow \mathbb{R}$ be an integrable scalar functional defined on \mathbb{T} , representing a local performance density of ${}^b_s\mathbf{H}(\boldsymbol{\theta})$ with left-invariant Riemannian metric. This local measure can be extended to a global measure $\mathcal{Z}(L_k)$ by integrating z over \mathbb{T} , yielding the following optimization problem on L_k :

$$\begin{aligned} \min_{L_k} \mathcal{Z}(L_k) &\triangleq \int_{\mathbb{T}} z({}^b_s\mathbf{H}(\boldsymbol{\theta}); L_k) \Omega_{\mathbb{T}} \\ \text{s.t.} \quad &\begin{cases} \nabla_{\boldsymbol{\theta}} \mathcal{E}(\boldsymbol{\theta}, \mathbf{b}) = 0, \mathbf{b} \in \mathbb{B} \\ \mathcal{C}(L_k) \leq 0 \end{cases} \end{aligned} \quad (18)$$

where $\Omega_{\mathbb{T}}$ represents the Riemannian volume form on \mathbb{T} induced from the Euclidean metric and $\mathcal{C}(L_k)$ denotes linear constraints on L_k . The equilibrium constraint restricts feasible configurations to the solution set $\mathbb{T}^* \triangleq \{\boldsymbol{\theta} \in \mathbb{T} \mid \nabla_{\boldsymbol{\theta}} \mathcal{E}(\boldsymbol{\theta}, \mathbf{b}) = \mathbf{0}\}$. If the actuation manifold \mathbb{B} is arbitrary, the set \mathbb{T}^* may not admit an explicit parametrization. Nevertheless, under mild regularity conditions on \mathcal{E} , and by Sard's theorem, the solution set $\mathbb{T}^* \subset \mathbb{T}$ is countably d -rectifiable, with $d = 3N - \text{rk}(\frac{\partial \boldsymbol{\theta}}{\partial \mathbb{B}})$. Hence, it admits a well-defined \mathcal{H}^d -measure and supports geometric integration. Consequently, the constrained integral over \mathbb{T} may be rewritten as an iterated integral over \mathbb{B} and the corresponding solution manifold:

$$\mathcal{Z}(L_k) = \int_{\mathbb{B}} \left(\int_{\mathbb{T}^*} z({}^b_s\mathbf{H}(\boldsymbol{\theta}); L_k) d\mathcal{H}^d(\boldsymbol{\theta}) \right) \Omega_{\mathbb{B}}.$$

Now, suppose the external magnetic field \mathbf{b} is spatially uniform with $\mathbf{b} = \mathbf{U}_u \mathbf{b}_u$ and satisfies the condition in Theorem 1. The manifold \mathbb{B} is now an affine subspace diffeomorphic to \mathbb{R}^3 . By Theorem 1, the stiffness matrix \mathbf{S} is nonsingular in a neighborhood of each $\mathbf{b}_u \in \mathbb{B}$. By Theorem 3, the Jacobian $\frac{\partial \boldsymbol{\theta}}{\partial \mathbb{B}} = \mathbf{S}^{-1} \mathbf{M}$ satisfies $\text{rk}(\mathbf{S}^{-1} \mathbf{M}) = 2N_m$, which ensures that $\frac{\partial \boldsymbol{\theta}}{\partial \mathbf{b}_u} = \mathbf{S}^{-1} \mathbf{M} \mathbf{U}_u$ is of full rank provided $N_m \geq 2$. In this regime, the equilibrium constraint gives rise to a smooth immersion $\boldsymbol{\theta}^* : \mathbb{B} \rightarrow \mathbb{T}$. The inner integral reduces to an evaluation at $\boldsymbol{\theta}^*(\mathbf{b})$, and using the area formula [44] yields:

$$\int_{\mathbb{T}^*} z({}^b_s\mathbf{H}(\boldsymbol{\theta}); L_k) d\mathcal{H}^d(\boldsymbol{\theta}) = z({}^b_s\mathbf{H}(\boldsymbol{\theta}); L_k) \mathcal{J}_{\boldsymbol{\theta}}(\mathbf{b}),$$

where $\mathcal{J}_{\boldsymbol{\theta}}(\mathbf{b})$ denotes the Jacobian of the immersion $\boldsymbol{\theta}^*(\mathbf{b})$ and is given by

$$\mathcal{J}_{\boldsymbol{\theta}} = \left[\det \left(\frac{\partial \boldsymbol{\theta}}{\partial \mathbf{b}_u} \right)^{\top} \frac{\partial \boldsymbol{\theta}}{\partial \mathbf{b}_u} \right]^{\frac{1}{2}} \triangleq [\det(\mathbf{G}_{\boldsymbol{\theta}})]^{\frac{1}{2}},$$

where $\mathbf{G}_{\boldsymbol{\theta}}$ denotes the Gram matrix of $\frac{\partial \boldsymbol{\theta}}{\partial \mathbf{b}_u}$. Substituting back, the global optimization problem (18) takes the following unconstrained reformulation:

$$\min_{L_k} \mathcal{Z}(L_k) = \int_{\mathbb{B}} z({}^b_s\mathbf{H}(\boldsymbol{\theta}^*(\mathbf{b})); L_k) \mathcal{J}_{\boldsymbol{\theta}} \Omega_{\mathbb{B}}. \quad (19)$$

The optimality is ensured by satisfying the following first-order necessary condition:

$$\begin{aligned} \nabla_{L_k} \mathcal{Z} &= \int_{\mathbb{B}} (z \nabla_{L_k} \mathcal{J}_{\boldsymbol{\theta}} + \mathcal{J}_{\boldsymbol{\theta}} \nabla_{L_k} z) \Omega_{\mathbb{B}} \\ &= \int_{\mathbb{B}} \left[\frac{1}{2} z \mathcal{J}_{\boldsymbol{\theta}} \text{tr}(\mathbf{G}_{\boldsymbol{\theta}}^{-1} \nabla_{L_k} \mathbf{G}_{\boldsymbol{\theta}}) + \mathcal{J}_{\boldsymbol{\theta}} \nabla_{L_k} z \right] \Omega_{\mathbb{B}} \\ &= 0, \quad \forall k \in \mathbb{K} / \{N_m - 1\}. \end{aligned}$$

Under regularity conditions, this implies the strong-form pointwise optimality condition:

$$\left(\frac{1}{2} z \text{tr}(\mathbf{G}_{\boldsymbol{\theta}}^{-1} \nabla_{L_k} \mathbf{G}_{\boldsymbol{\theta}}) + \nabla_{L_k} z \right) \mathcal{J}_{\boldsymbol{\theta}} = 0, \quad \forall \mathbf{b}_u \in \mathbb{B}. \quad (20)$$

Observed that the condition trivially holds when $\mathcal{J}_{\boldsymbol{\theta}} = 0$. However, the collapse of immersion Jacobian results in a degenerate configuration. That is, the embedded magnets may have merged or be unable to generate torques. Since $\mathcal{J}_{\boldsymbol{\theta}}$ contains complex Hessian terms, we first derive a tractable approximation to facilitate further analysis.

Lemma 3. *Suppose the inequality condition in Theorem 1 holds. Then the immersion Jacobian admits the expansion*

$$\begin{aligned} \mathcal{J}_{\boldsymbol{\theta}}^2 &= \det(\mathbf{U}_u^{\top} \mathbf{M}^{\top} \boldsymbol{\Lambda}^{-2} \mathbf{M} \mathbf{U}_u) + \epsilon \\ &\triangleq \tilde{\mathcal{J}}_{\boldsymbol{\theta}}^2 + \epsilon \end{aligned} \quad (21)$$

where the remainder term ϵ is bounded above as

$$|\epsilon| \leq \frac{3(2\mathcal{L} - \mathcal{L}^2) N_m^3 \mathcal{M}_0^6}{(1 - \mathcal{L})^2 \Lambda_{\min}^6},$$

and satisfies $\lim_{B_k \rightarrow 0} |\epsilon| \rightarrow 0$.

Proof. The proof is deferred to the supplementary material. ■

It shows that $\tilde{\mathcal{J}}_{\boldsymbol{\theta}}$ provides a close approximation of $\mathcal{J}_{\boldsymbol{\theta}}$ in the weak-field regime, with the residual term converging to zero as the magnetic field strength decreases. We can now turn to analyze the approximation of the objective $\tilde{\mathcal{Z}}(L_k) \triangleq \int_{\mathbb{B}} z \tilde{\mathcal{J}}_{\boldsymbol{\theta}} \Omega_{\mathbb{B}}$. Let $\mathbf{M}(\boldsymbol{\theta})$ in (12) be represented as $\mathbf{M} = \mathbf{D}_{k_{N_m-1}}^{\top} \mathbf{U}_m \mathbf{D}_m$, we notice

$$\mathbf{U}_m^{\top} \mathbf{D}_{k_{N_m-1}} \boldsymbol{\Lambda}^{-2} \mathbf{D}_{k_{N_m-1}}^{\top} \mathbf{U}_m = \mathbf{U}_m^{\top} \boldsymbol{\Lambda}^{-2} \mathbf{U}_m = \boldsymbol{\Lambda}_m \otimes \mathbf{I}_3$$

where

$$\boldsymbol{\Lambda}_m = \begin{bmatrix} \Lambda_{k_0}^m & \Lambda_{k_0}^m & \dots & \Lambda_{k_0}^m \\ \Lambda_{k_0}^m & \Lambda_{k_1}^m & \dots & \Lambda_{k_1}^m \\ \vdots & \vdots & \ddots & \vdots \\ \Lambda_{k_0}^m & \Lambda_{k_1}^m & \dots & \Lambda_{k_{N_m-1}}^m \end{bmatrix} \in \mathbb{R}^{N_m \times N_m}$$

with $\Lambda_{k_i}^m = \sum_{j=0}^{k_i} \frac{\ell_j^2}{E_j^2 I_j^2} \approx \frac{1}{k_0 E^2 I^2} \sum_{j=0}^i (L_{k_j} - L_{k_{j-1}})^2$ as a function of L_k . The following lemma shows the relation between the singularity of $\tilde{\mathcal{J}}_\theta$ and the configuration of L_k :

Lemma 4. *Suppose the embedded magnets are placed at the two boundaries (proximal and distal ends), that is $\forall 0 \leq N_k < N_m - 1$, $L_{k_{N_k}} = 0$ and $L_{k_{N_k+1}} = L$. Then $\tilde{\mathcal{J}}_\theta = 0$.*

Proof. Under the assumed boundary placement, it is simplified that $\Lambda_m \otimes \mathbf{I}_3 = \Lambda_{k_{N_m-1}}^m (\mathbf{v} \otimes \mathbf{I}_3) (\mathbf{v}^\top \otimes \mathbf{I}_3)$, where $\mathbf{v} = [\mathbf{0}_{N_k}^\top, \mathbf{1}_{N_m-N_k}^\top]^\top$. Substituting this into the expression for $\tilde{\mathcal{J}}_\theta$, we obtain

$$(\mathbf{v}^\top \otimes \mathbf{I}_3) \mathbf{U}_u \mathbf{D}_m = \sum_{i=N_k+1}^{N_m-1} [\mathbf{m}_{k_i}]_\times = \left[\sum_{i=N_k+1}^{N_m-1} \mathbf{m}_{k_i} \right]_\times.$$

Consequently, the rank of the expression for $\tilde{\mathcal{J}}_\theta$ shows that

$$\begin{aligned} & \text{rk}(\mathbf{U}_u^\top \mathbf{D}_m^\top (\Lambda_m \otimes \mathbf{I}_3) \mathbf{U}_u \mathbf{D}_m) \\ &= \text{rk}((\mathbf{v}^\top \otimes \mathbf{I}_3) \mathbf{U}_u \mathbf{D}_m) = \text{rk} \left(\left[\sum_{i=N_k+1}^{N_m-1} \mathbf{m}_{k_i} \right]_\times \right) \leq 2. \end{aligned}$$

That is, the actuation mapping becomes deficient in rank, and we conclude that $\tilde{\mathcal{J}}_\theta = 0$. ■

Lemma 4 indicates that placing all embedded magnets at boundary positions leads to a singularity in $\tilde{\mathcal{J}}_\theta$, as expected. This degeneration of the measure can also be interpreted in terms of an effective reduction in the number of independent magnets. Specifically, magnets located at the proximal end have no actuation effect, while those at the distal end act collectively as a single unit. As a result, under boundary-concentrated configurations, the effective number of embedded magnets is reduced to one. From Theorem 3, we notice $\text{rk}(\mathbf{M}(\theta)) = 2$ when $N_m = 1$, and the Jacobian $\frac{\partial \theta}{\partial \mathbf{b}_u}$ becomes deficient in rank, leading to a singularity of immersion Jacobian. This structural degeneracy provides a tractable mechanism for determining the optimal solution to a class of objective functions, as formalized in the following theorem.

Theorem 5. *If the performance index satisfies $z(\mathbf{b}_u; L_k) > 0$, and the structural parameter L_k satisfies the boundary configuration condition in Lemma 4, then the objective $\tilde{\mathcal{Z}}(L_k)$ attains its minimum at this configuration.*

Proof. Since $z > 0$ and $\tilde{\mathcal{J}}_\theta \geq 0$, it follows that $\tilde{\mathcal{Z}}(L_k) \geq 0$ for any admissible L_k . When L_k satisfies the boundary configuration condition in Lemma 4, we have $\tilde{\mathcal{J}}_\theta(\mathbf{b}) \equiv 0$ over \mathbb{B} , and thus $\tilde{\mathcal{Z}}(L_k) = 0$. ■

Due to the Jacobian singularity at boundary configurations, the value of the objective becomes insensitive to the gradient of the performance index, thereby weakening the meaningfulness of the solution. However, the minimum spacing constraint prevents the structural parameter L_k from reaching such degenerate configurations. Since \mathcal{J}_θ remains continuous on L_k , it stays small in the vicinity of the boundary, making nearby configurations highly competitive in minimizing the objective. In this case, the performance gradient becomes the key factor in selecting specific configurations. One can also

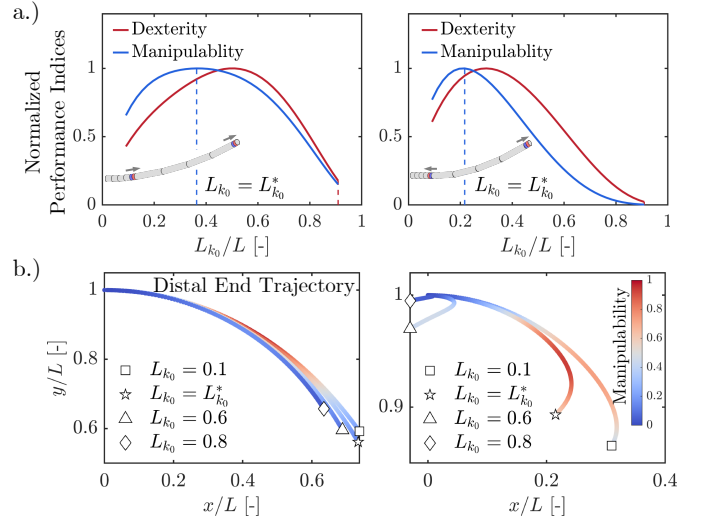


Fig. 6. a.) Normalized manipulability and dexterity of MeSCRs with two embedded magnets as functions of normalized magnet position $L_{k_0}/L \in [0, 1]$: (left) aligned magnetic moments, (right) opposing magnetic moments. b.) Distal end trajectories under various magnet placements L_{k_0}/L and moments. Color gradient encodes normalized local manipulability.

reduce the optimization bias by considering the objective as \mathcal{Z}/\mathcal{V} , where $\mathcal{V} \triangleq \int_{\mathbb{B}} \mathcal{J}_\theta \Omega_{\mathbb{B}}$ is the total induced volume. This normalized objective reflects the average performance on the configuration space and is insensitive to Jacobian singularity.

Now we focus on the nontrivial solution of (20). If z is a non-zero performance index, one can further deduce that

$$\text{tr}(\mathbf{G}_\theta^{-1} \nabla_{L_k} \mathbf{G}_\theta) = \sum_i \frac{\nabla_{L_k} \lambda_i(\mathbf{G}_\theta)}{\lambda_i(\mathbf{G}_\theta)} = -2 \frac{\nabla_{L_k} z}{z}. \quad (22)$$

Geometrically, this condition implies that optimizing the local performance requires structurally modulating the spectrum of the configuration space metric to counteract its distortion. From Lemma 3, we have the following approximation:

$$\begin{aligned} \mathbf{G}_\theta &\approx \mathbf{U}_u^\top \mathbf{D}_m^\top (\Lambda_m \otimes \mathbf{I}_3) \mathbf{D}_m \mathbf{U}_u \\ &= \sum_{ij} \Lambda_{ij}^m \left(\mathbf{m}_{k_i} \mathbf{m}_{k_j}^\top - (\mathbf{m}_{k_i}^\top \mathbf{m}_{k_j}) \mathbf{I}_3 \right) \end{aligned} \quad (23)$$

in which $\mathbf{m}_k = M(\cos(\theta_0^k) \bar{\mathbf{t}} - \sin(\theta_0^k) \mathbf{v})$. While the spectrum is analytically elusive for general $\mathbf{v} \in \mathbb{S}^2$, closed-form expressions are still available in the following cases.

1) *Analytical Example:* Consider a MeSCR with two axially embedded magnets actuated by a spatially uniform field $\mathbf{b}_u \in \Pi$ with $\mathbf{v}^\top \bar{\mathbf{t}} = 0$, where the global manipulability is to be maximized [23]. The two magnets have identical dipole strength. Let one magnet be fixed at the distal end ($L_{k_1} = L$), while the position of the other magnet L_{k_0} serves as the design variable, subject to the boundary constraint $0 < L_{k_0} < L$. From Corollary 1, the joint variable simplifies to $\theta_i = \theta_i \mathbf{n}$. In this configuration, the MeSCR becomes kinematically equivalent to a planar N -joint revolute open-chain mechanism. Let $\theta_i^j \triangleq \sum_{l=i}^j \theta_l$ denote the cumulative joint angle. In the regime of weak magnetic actuation, the global manipulability index has the linearized expression on $\theta_{k_0}^{k_1}$: $z \approx L_{k_0}(L - L_{k_0}) \left| \theta_{k_0}^{k_1} \right|$, where the analytical form is

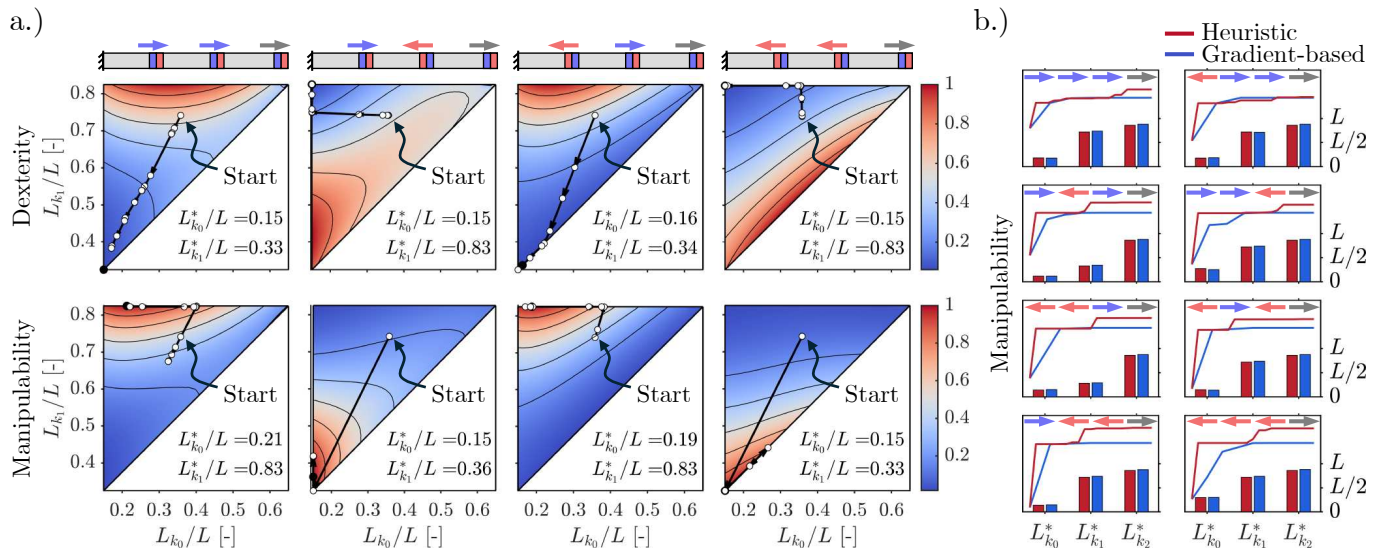


Fig. 7. a.) Optimization results under 2^2 magnetic orientation combinations. The background color maps represent normalized performance values obtained via exhaustive search. Black lines indicate trajectories of the gradient-based optimization. b.) Optimization results across 2^3 magnetic orientations, comparing the gradient-based method with a heuristic method. Bar plots show the configuration at optimized manipulability with convergence curves overlaid.

derived from the planar 2-joint revolute open-chain mechanism. Similarly, applying the approximate \mathbf{G}_m from (23), the immersion Jacobian also admits the linearized form:

$$\mathcal{J}_\theta \approx \begin{cases} M^3 \sqrt{\Lambda_{k_0}^m (\Lambda_{k_1}^m - \Lambda_{k_0}^m) (3\Lambda_{k_0}^m + \Lambda_{k_1}^m)} \left| \theta_{k_0}^{k_1} \right|, & \text{if } \bar{\mathbf{m}}_{k_0} = \bar{\mathbf{m}}_{k_1}, \\ M^3 \sqrt{\Lambda_{k_0}^m (\Lambda_{k_1}^m - \Lambda_{k_0}^m)} \left| \theta_{k_0}^{k_1} \right|, & \text{if } \bar{\mathbf{m}}_{k_0} = -\bar{\mathbf{m}}_{k_1}, \end{cases}$$

The cumulative rotation angle can also be approximated using (17) as $\left| \theta_{k_0}^{k_1} \right| \approx \frac{L - L_{k_0}}{EI} \left| \bar{\mathbf{m}}_k^\top [\mathbf{b}_u] \times \mathbf{n} \right|$. Substituting this into the above expressions for z and \mathcal{J}_θ , we can factor the dependence on L_{k_0} out of the integral in the objective. The structural optimization problem thus reduces to:

$$\max_{L_{k_0}} \begin{cases} L_{k_0}^2 (L - L_{k_0})^4 \sqrt{4L_{k_0}^2 + (L - L_{k_0})^2}, & \text{if } \bar{\mathbf{m}}_{k_0} = \bar{\mathbf{m}}_{k_1}, \\ L_{k_0}^2 (L - L_{k_0})^5, & \text{if } \bar{\mathbf{m}}_{k_0} = -\bar{\mathbf{m}}_{k_1}. \end{cases}$$

Then, the optimal magnet placement is obtained by using the first-order necessary condition as

$$L_{k_0}^* \approx \begin{cases} 0.368L, & \text{if } \bar{\mathbf{m}}_{k_0} = \bar{\mathbf{m}}_{k_1}, \\ \frac{2}{7}L, & \text{if } \bar{\mathbf{m}}_{k_0} = -\bar{\mathbf{m}}_{k_1}. \end{cases}$$

The result is entirely determined by the structural geometry, independent of material or actuation parameters, and thus exhibits scale invariance. Interestingly, when $\bar{\mathbf{m}}_{k_0} = \bar{\mathbf{m}}_{k_1}$, the ratio of optimal placement $L/L_{k_0}^* \approx 2.718$ is numerically close to Euler's number, suggesting a geometric correspondence with the logarithmic spiral structures widely employed in soft continuum design.

We also evaluated the kinematic dexterity of the MeSCR through minimizing the distortion as defined in [24]. It is easy to verify that the distortion density satisfies the assumption of Theorem 5. Thus, we deduce that the optimal configuration of embedded magnets has a boundary distribution. We show numerical simulation results of normalized manipulability and

dexterity in Fig. 6a. When the magnetic moments are aligned (left graph), the configuration that maximizes manipulability exhibits good agreement with the theoretical result. In contrast, the opposing case (right graph) shows a deviation, which may be attributed to stronger nonlinearity in the index. For both cases, the configurations that minimize distortion consistently place the embedded magnet at the distal end, as expected. Fig. 6b illustrates the reachable distal trajectories under varying magnet placements. Although the optimal placements yield high manipulability along the path, their spatial extent remains limited. This apparent disparity underscores the geometric distinction between local controllability and global reachability, while the latter pertains to the image of the equilibrium map over the actuation submanifold. Therefore, any attempt to maximize overall performance must reconcile the trade-off between local dexterity and global coverage, as the two are not generally aligned.

2) *Numerical Examples:* For MeSCRs with three or more embedded magnets, deriving a closed-form solution to the optimization problem becomes increasingly intractable. In such cases, we resort to a gradient-based optimization scheme, leveraging the analytical gradient expression provided in (22). Fig. 7a illustrates the optimization trajectories for representative cases with four possible direction combinations. The background colormaps depict the globally normalized performance values obtained via exhaustive enumeration. Across all cases, the gradient-based method consistently converges to configurations that match the global optima, demonstrating its reliability and consistency with full search results.

Moreover, the optimized magnet placements for maximizing dexterity closely follow the geometric insights established in Theorem 5. In all observed cases, the optimizer implicitly minimizes the net torque induced by the embedded magnets. Specifically, when adjacent magnets are aligned, the solution tends to separate them spatially to avoid torque

amplification, whereas when they are oppositely oriented, the optimizer brings them closer to enable partial cancellation. These outcomes suggest that the dexterity metric inherently penalizes unbalanced torque distributions that restrict the range of achievable actuation directions.

As shown in Fig. 7b, the heuristic and gradient-based optimization methods yield consistent results both in terms of optimal configuration and convergence behaviors. Combining with the performance maps in Fig. 7a, it demonstrates that manipulability is highly sensitive to the spatial layout and directions of the embedded magnets. In some cases, optimal configurations are observed when magnets are distributed farther apart, highlighting the benefit of spatially diverse actuation sources. In comparison to dexterity, manipulability optimization focuses on maximizing the volume of attainable motion directions. As a result, the optimizer may favor configurations that introduce local torque in exchange for broader kinematic responsiveness.

IV. CONCLUSION AND DISCUSSION

This paper presents a unified framework for modeling and optimizing the kinematic performance of multi-magnet embedded soft continuum robots. The proposed EPRB model enables a differentiable representation of equilibrium configurations under magnetic actuation, and supports explicit expressions for both the manipulator Jacobian and Hessian in multi-magnet settings. The analysis of equilibrium well-posedness yields sufficient conditions for solution uniqueness and continuity under bounded actuation, offering a means to ensure continuous configuration tracking in quasi-static operations. The upper bound on controllable degrees of freedom, shown to be twice the number of embedded magnets, offers a simple yet practical rule for relating design parameters to task-space controllability.

A key contribution of this paper lies in the development of a differential geometric optimization framework, where classical kinematic measures are reparametrized over the actuation space via equilibrium immersions. This approach accommodates a wide range of performance criteria, including but not limited to manipulability and dexterity, and admits both analytic and gradient-based solution methods. Although demonstrated in the context of MeSCRs, the formulation applies more broadly to continuum structures actuated by distributed torques, and may offer guidance in the design of other soft or compliant mechanisms where actuation and configuration are implicitly coupled.

APPENDIX A PROOFS OF PROPOSITIONS

A. Proof of Proposition 1

Noticing that

$$\begin{aligned} \|\mathbf{M}_i(\boldsymbol{\theta})\mathbf{b}\| &= \left\| \sum_{k \in \mathbb{K}, k \geq i} \left([\mathbf{m}_k]_{\times}^{\top} \mathbf{R}_0^i \mathbf{J}_{\mathbf{R}_r}^{\theta_i} \right)^{\top} \mathbf{b}(\mathbf{p}_k) \right\| \\ &\leq \left\| \mathbf{R}_0^i \mathbf{J}_{\mathbf{R}_r}^{\theta_i} \right\| \sum_{k \in \mathbb{K}, k \geq i} \left\| [\mathbf{m}_k]_{\times} \mathbf{b}(\mathbf{p}_k) \right\| \\ &= \sum_{k \in \mathbb{K}, k \geq i} M_k B_k \triangleq \mathcal{M}_i, \end{aligned}$$

it is convenient to obtain:

$$\|\mathbf{M}(\boldsymbol{\theta})\mathbf{b}\| = \sqrt{\sum_{i=0}^{N-1} \|\mathbf{M}_i(\boldsymbol{\theta})\mathbf{b}\|^2} \leq \sqrt{\sum_{i=0}^{N-1} \mathcal{M}_i^2} \triangleq \mathcal{M},$$

and

$$\|\mathbf{M}(\boldsymbol{\theta})\| = \sqrt{\sum_{i=0}^{N-1} \|\mathbf{M}_i(\boldsymbol{\theta})\|^2} \leq \sqrt{N_m k_{N_m-1}} \max_k M_k \triangleq \mathcal{M}_0.$$

B. Proof of Proposition 2

Given that the Hessian matrix is symmetric, it can be expressed equivalently as

$$\frac{\partial^2 \mathcal{E}_m}{\partial \boldsymbol{\theta} \partial \boldsymbol{\theta}^{\top}} = \sum_{k \in \mathbb{K}} \text{sym} \left(\mathbf{D}_k^{\top} \mathbf{C}_k \mathbf{D}_k + \mathbf{Q}^k \right) \triangleq \mathbf{S}_m.$$

Whence,

$$\mathbf{D}_k = \text{blkdiag} \left\{ \mathbf{R}_0 \mathbf{J}_{\mathbf{R}_r}^{\theta_0}, \dots, \mathbf{R}_0^k \mathbf{J}_{\mathbf{R}_r}^{\theta_k}, \underbrace{\mathbf{0}_{3 \times 3}, \dots, \mathbf{0}_{3 \times 3}}_{N-k-1} \right\}, \quad (24)$$

$$\mathbf{Q}^k = \text{blkdiag} \left\{ \mathbf{Q}_0, \dots, \mathbf{Q}_k, \underbrace{\mathbf{0}_{3 \times 3}, \dots, \mathbf{0}_{3 \times 3}}_{N-k-1} \right\},$$

and

$$\mathbf{C}_k = \text{blkdiag} \left\{ 2\mathbf{U}_{k \times k} - \mathbf{I}_{k \times k}, \underbrace{\mathbf{0} \dots \mathbf{0}}_{N-k-1} \right\} \otimes \left([\mathbf{b}_k]_{\times}^{\top} [\mathbf{m}_k]_{\times} \right)$$

with $\mathbf{U}_{k \times k}$ denotes the upper triangle matrix with all elements equal to 1 and \otimes denotes the Kronecker product. Then, using the triangle inequality and sub-multiplicative property, the following inequality holds for the spectrum norm of the Hessian matrix:

$$\begin{aligned} \|\mathbf{S}_m\| &= \left\| \sum_{k \in \mathbb{K}} \text{sym} \left\{ \mathbf{D}_k^{\top} \mathbf{C}_k \mathbf{D}_k + \mathbf{Q}^k \right\} \right\| \\ &\leq \sum_{k \in \mathbb{K}} \|\mathbf{D}_k^{\top}\| \|\mathbf{C}_k\| \|\mathbf{D}_k\| + \|\mathbf{Q}^k\| \\ &= \sum_{k \in \mathbb{K}} \|\mathbf{C}_k\| + \|\mathbf{Q}^k\| \end{aligned} \quad (25)$$

where we used the fact that $\|\mathbf{D}_k^{\top}\| = \|\mathbf{D}_k\| = 1$. The spectrum norm of \mathbf{C}_k is straightforward to be given by

$$\begin{aligned} \|\mathbf{C}_k\| &= \|2\mathbf{U}_{k \times k} - \mathbf{I}_{k \times k}\| \left\| [\mathbf{b}_k]_{\times}^{\top} [\mathbf{m}_k]_{\times} \right\| \\ &\leq \frac{4k}{\pi} \|\mathbf{b}_k\| \|\tilde{\mathbf{m}}_k\| = \frac{4k}{\pi} M_k B_k \end{aligned} \quad (26)$$

For small rotation angles, we note that

$$\lim_{\boldsymbol{\theta} \rightarrow \mathbf{0}} \|\mathbf{Q}^k\| = \lim_{\boldsymbol{\theta} \rightarrow \mathbf{0}} \max_{i=0, \dots, k} \{\|\mathbf{Q}_i\|\} = 0. \quad (27)$$

Combing (25), (26), and (27), the Jacobian of the vector-valued function $\mathbf{M}(\boldsymbol{\theta})\mathbf{b}$ satisfies:

$$\left\| \frac{\partial}{\partial \boldsymbol{\theta}} \mathbf{M}(\boldsymbol{\theta})\mathbf{b} \right\| = \|\mathbf{S}_m\| \leq \sum_{k \in \mathbb{K}} \frac{4k}{\pi} M_k B_k \triangleq \mathcal{L}.$$

Therefore, the function is Lipschitz continuous on \mathbb{R}^{3N} with the Lipschitz constant \mathcal{L} .

REFERENCES

- [1] Z. Yang, H. Yang, Y. Cao, Y. Cui, and L. Zhang, "Magnetically actuated continuum medical robots: A review," *Advanced intelligent systems*, vol. 5, no. 6, p. 2200416, 2023.
- [2] Z. Yang, L. Yang, M. Zhang, C. Zhang, S. C. H. Yu, and L. Zhang, "Ultrasound-guided catheterization using a driller-tipped guidewire with combined magnetic navigation and drilling motion," *IEEE/ASME Transactions on Mechatronics*, vol. 27, no. 5, pp. 2829–2840, Oct. 2022.
- [3] W. Peng, H. Xie, S. Zhang, and L. Gu, "Inverse kinematic analysis and agile control of a magnetically actuated catheter," *Robotics and Computer-Integrated Manufacturing*, vol. 86, p. 102662, Apr. 2024.
- [4] Z. Li, J. Li, Z. Wu, Y. Chen, M. Yeerbulati, and Q. Xu, "Design and hierarchical control of a homocentric variable stiffness magnetic catheter for multi-arm robotic ultrasound-assisted coronary intervention," *IEEE Transactions on Robotics*, pp. 1–20, 2024.
- [5] J. Sikorski, C. M. Heunis, R. Obeid, V. K. Venkiteswaran, and S. Misra, "A flexible catheter system for ultrasound-guided magnetic projectile delivery," *IEEE Transactions on Robotics*, vol. 38, no. 3, pp. 1959–1972, Jun. 2022.
- [6] O. Oniku and D. Arnold, "High-energy-density permanent micromagnets formed from heterogeneous magnetic powder mixtures," in *2012 IEEE 25th International Conference on Micro Electro Mechanical Systems (MEMS)*. IEEE, 2012, pp. 436–439.
- [7] V. N. Le, N. H. Nguyen, K. Alameh, R. Weerasooriya, and P. Pratten, "Accurate modeling and positioning of a magnetically controlled catheter tip," *Medical physics*, vol. 43, no. 2, pp. 650–663, 2016.
- [8] J. Park, H. Kee, and S. Park, "Workspace expansion of magnetic soft continuum robot using movable opposite magnet," *IEEE ROBOTICS AND AUTOMATION LETTERS*, vol. 9, no. 7, pp. 6648–6655, Jul. 2024.
- [9] Y. Cao, Z. Yang, B. Hao, X. Wang, M. Cai, Z. Qi, B. Sun, Q. Wang, and L. Zhang, "Magnetic continuum robot with intraoperative magnetic moment programming," *Soft Robotics*, vol. 10, no. 6, pp. 1209–1223, 2023.
- [10] D. Lin, N. Jiao, Z. Wang, and L. Liu, "A magnetic continuum robot with multi-mode control using opposite-magnetized magnets," *IEEE Robotics and Automation Letters*, vol. 6, no. 2, pp. 2485–2492, Apr. 2021.
- [11] M. Zhang, L. Yang, H. Yang, L. Su, J. Xue, Q. Wang, B. Hao, Y. Jiang, K. F. Chan, J. J. Y. Sung *et al.*, "A magnetically actuated microcatheter with soft rotatable tip for enhanced endovascular access and treatment efficiency," *Science advances*, vol. 11, no. 25, p. eadv1682, 2025.
- [12] T. Da Veiga, J. H. Chandler, P. Lloyd, G. Pittiglio, N. J. Wilkinson, A. K. Hoshiar, R. A. Harris, and P. Valdastrì, "Challenges of continuum robots in clinical context: A review," *Progress in Biomedical Engineering*, vol. 2, no. 3, p. 032003, Aug. 2020.
- [13] J. Edelmann, A. J. Petruska, and B. J. Nelson, "Magnetic control of continuum devices," *The International Journal of Robotics Research*, vol. 36, no. 1, pp. 68–85, Jan. 2017.
- [14] L. B. Kratchman, T. L. Bruns, J. J. Abbott, and R. J. Webster, "Guiding elastic rods with a robot-manipulated magnet for medical applications," *IEEE Transactions on Robotics*, vol. 33, no. 1, pp. 227–233, 2017.
- [15] R. J. Roesthuis and S. Misra, "Steering of multisegment continuum manipulators using rigid-link modeling and fbg-based shape sensing," *IEEE Transactions on Robotics*, vol. 32, no. 2, pp. 372–382, Apr. 2016.
- [16] T. Greigarn and M. C. Çavuşoğlu, "Pseudo-rigid-body model and kinematic analysis of mri-actuated catheters," in *2015 IEEE International Conference on Robotics and Automation (ICRA)*, May 2015, pp. 2236–2243.
- [17] Y. Cao, M. Cai, B. Sun, Z. Qi, J. Xue, Y. Jiang, B. Hao, J. Zhu, X. Liu, C. Yang, and L. Zhang, "Magnetic continuum robot with modular axial magnetization: Design, modeling, optimization, and control," *IEEE Transactions on Robotics*, vol. 41, pp. 1513–1532, 2025.
- [18] J. Sikorski, A. Denasi, G. Bucchi, S. Scheggi, and S. Misra, "Vision-based 3-d control of magnetically actuated catheter using bigmag—an array of mobile electromagnetic coils," *IEEE/ASME Trans. Mechatron.*, vol. 24, no. 2, pp. 505–516, Apr. 2019.
- [19] G. Pittiglio, A. L. Orekhov, T. da Veiga, S. Calò, J. H. Chandler, N. Simaan, and P. Valdastrì, "Closed loop static control of multi-magnet soft continuum robots," *IEEE Robotics and Automation Letters*, vol. 8, no. 7, pp. 3980–3987, Jul. 2023.
- [20] D. Lin, W. Chen, K. He, N. Jiao, Z. Wang, and L. Liu, "Position and orientation control of multisection magnetic soft microcatheters," *IEEE/ASME Transactions on Mechatronics*, vol. 28, no. 2, pp. 907–918, Apr. 2023.
- [21] D. Lin, N. Li, N. Jiao, Z. Wang, and L. Liu, "Kinematic analysis of multi-section opposite magnetic catheter robots with solution multiplicity," *IEEE Transactions on Automation Science and Engineering*, pp. 1–12, 2022.
- [22] L. Wang, Y. Kim, C. F. Guo, and X. Zhao, "Hard-magnetic elastica," *Journal of the Mechanics and Physics of Solids*, vol. 142, p. 104045, Sep. 2020.
- [23] T. Yoshikawa, "Manipulability of robotic mechanisms," *The international journal of Robotics Research*, vol. 4, no. 2, pp. 3–9, 1985.
- [24] F. C. Park and R. W. Brockett, "Kinematic dexterity of robotic mechanisms," *The International Journal of Robotics Research*, vol. 13, no. 1, pp. 1–15, Feb. 1994.
- [25] O. M. O'Reilly, *Modeling Nonlinear Problems in the Mechanics of Strings and Rods*, ser. Interaction of Mechanics and Mathematics. Cham: Springer International Publishing, 2017.
- [26] G. Pittiglio, A. L. Orekhov, T. da Veiga, S. Calò, J. H. Chandler, N. Simaan, and P. Valdastrì, "Closed loop static control of multi-magnet soft continuum robots," *IEEE Robotics and Automation Letters*, vol. 8, no. 7, pp. 3980–3987, 2023.
- [27] T. D. Barfoot and P. T. Furgale, "Associating uncertainty with three-dimensional poses for use in estimation problems," *IEEE Transactions on Robotics*, vol. 30, no. 3, pp. 679–693, 2014.
- [28] J. Rychlewski, "On hooke's law," *Journal of Applied Mathematics and Mechanics*, vol. 48, no. 3, pp. 303–314, 1984.
- [29] M. Richter, V. K. Venkiteswaran, and S. Misra, "Concentric tube-inspired magnetic reconfiguration of variable stiffness catheters for needle guidance," *IEEE Robotics and Automation Letters*, pp. 1–8, 2023.
- [30] G. S. Chirikjian, *Stochastic Models, Information Theory, and Lie Groups, Volume 2: Analytic Methods and Modern Applications*. Springer Science & Business Media, Nov. 2011.
- [31] L. Lu, J. Sim, and R. R. Zhao, "Mechanics of hard-magnetic soft materials: A review," *Mechanics of Materials*, p. 104874, 2023.
- [32] Z. Wu and J. Zhang, "Closed-loop magnetic control of medical soft continuum robots for deflection," *IEEE/ASME Transactions on Mechatronics*, pp. 1–12, 2024.
- [33] I. Tunay, "Position control of catheters using magnetic fields," in *Proceedings of the IEEE International Conference on Mechatronics, 2004. ICM '04.*, Jun. 2004, pp. 392–397.
- [34] Z. Wu, J. Zhang, S. Wei, and D. Chen, "Kirchhoff rod-based three-dimensional dynamical model and real-time simulation for medical-magnetic guidewires," *Computer Methods and Programs in Biomedicine*, vol. 240, p. 107646, Oct. 2023.
- [35] M. Richter, V. K. Venkiteswaran, and S. Misra, "Multi-point orientation control of discretely-magnetized continuum manipulators," *IEEE Robotics and Automation Letters*, vol. 6, no. 2, pp. 3607–3614, Apr. 2021.
- [36] T. Greigarn, N. L. Poirot, X. Xu, and M. C. Çavuşoğlu, "Jacobian-based task-space motion planning for mri-actuated continuum robots," *IEEE Robotics and Automation Letters*, vol. 4, no. 1, pp. 145–152, Jan. 2019.
- [37] G. Pittiglio, P. Lloyd, T. da Veiga, O. Onaizah, C. Pompili, J. H. Chandler, and P. Valdastrì, "Patient-specific magnetic catheters for atraumatic autonomous endoscopy," *SOFT ROBOTICS*, vol. 9, no. 6, pp. 1120–1133, Dec. 2022.
- [38] V. T. Le, "Accurate modelling and positioning of a magnetically-controlled catheter tip," Ph.D. dissertation, Edith Cowan University, 2015, retrieved from <https://ro.ecu.edu.au/theses/1711>. [Online]. Available: <https://ro.ecu.edu.au/theses/1711>
- [39] G. Pittiglio, M. Mencattelli, A. Donder, Y. Chitalia, and P. E. Dupont, "Hybrid tendon and ball chain continuum robots for enhanced dexterity in medical interventions," in *2023 IEEE/RSJ International Conference on Intelligent Robots and Systems (IROS)*. IEEE, 2023, pp. 8461–8466.
- [40] K. J. Chun, E. Wissner, B. Koekuerk, M. Konstantinidou, B. Schmidt, T. Zerm, A. Metzner, R. Tilz, S. Boczor, A. Fuernkranz *et al.*, "Remote-controlled magnetic pulmonary vein isolation using a new irrigated-tip catheter in patients with atrial fibrillation," *Circulation: Arrhythmia and Electrophysiology*, vol. 3, no. 5, pp. 458–464, 2010.
- [41] B. Webster, "Biosense webster products catalogue 2020," 2020, accessed: 2024-10-30. [Online]. Available: https://www.njmedtech.com/sites/default/files/user_uploaded_assets/pdf_assets/2020-09/084962-200128%20EMEA%20Biosense_Products_Catalogue_2020_single_page.pdf
- [42] Q. Boehler, S. Gervasoni, S. L. Charreyron, C. Chautems, and B. J. Nelson, "On the workspace of electromagnetic navigation systems," *IEEE Transactions on Robotics*, pp. 1–17, 2022.
- [43] Y. Huang, Q. Zhao, J. Hu, and H. Liu, "Design and modeling of a multi-dof magnetic continuum robot with diverse deformation modes," *IEEE Robotics and Automation Letters*, vol. 9, no. 4, pp. 3956–3963, Apr. 2024.
- [44] H. Federer, *Geometric measure theory*. Springer, 2014.

Supplementary Material for “Unified Modeling and Structural Optimization of Multi-magnet Embedded Soft Continuum Robots for Enhanced Kinematic Performances”

This supplemental document provides additional materials to support the results presented in the main manuscript.

S.I. HESSIANS OF THE MAGNETIC POTENTIAL ENERGY

The Hessian of \mathcal{E}_m is known as symmetric. It is convenient to present the matrix in parts. A portion of the Hessian has the following representation:

$$\frac{\partial^2 \mathcal{E}_m}{\partial \boldsymbol{\theta}_i \partial \boldsymbol{\theta}_i^\top} = \sum_{k \in \mathbb{K}, k \geq i} \text{sym} \left(\mathbf{J}_{\mathbf{R}_l}^{\boldsymbol{\theta}_i} \mathbf{R}_0^{i\top} [\mathbf{b}_k]^\top [\mathbf{m}_k]_\times \mathbf{R}_0^i \mathbf{J}_{\mathbf{R}_r}^{\boldsymbol{\theta}_i} + \mathbf{Q}_i(\boldsymbol{\theta}_i, \boldsymbol{\rho}_i) \right)$$

where $\mathbf{J}_{\mathbf{R}_l}^{\boldsymbol{\theta}_i}$ is the left Jacobian of the SO(3) manifold that $\mathbf{J}_{\mathbf{R}_l}^{\boldsymbol{\theta}_i} = (\mathbf{J}_{\mathbf{R}_r}^{\boldsymbol{\theta}_i})^\top$, and

$$\begin{aligned} \mathbf{Q}_i(\boldsymbol{\theta}_i, \boldsymbol{\rho}_i) &= \left(2 \frac{\theta_i - \sin \theta_i}{\theta_i^3} - \frac{1 - \cos \theta_i}{\theta_i^2} \right) ([\boldsymbol{\theta}_i]_\times [\boldsymbol{\rho}_i]_\times) \\ &\quad - \left(\frac{\theta_i - \sin \theta_i}{\theta_i^3} + 2 \frac{1 - \cos \theta_i - \frac{1}{2} \theta_i^2}{\theta_i^4} \right) ([\boldsymbol{\theta}_i]_\times^2 [\boldsymbol{\rho}_i]_\times) \\ &\quad - \left(\frac{1 - \cos \theta_i - \frac{1}{2} \theta_i^2}{\theta_i^4} - 3 \frac{\theta_i - \sin \theta_i - \frac{1}{6} \theta_i^3}{\theta_i^5} \right) \\ &\quad \times ([\boldsymbol{\theta}_i]_\times [\boldsymbol{\rho}_i]_\times [\boldsymbol{\theta}_i]_\times^2) \end{aligned}$$

is the derivative matrix of $\mathbf{J}_{\mathbf{R}_l}^{\boldsymbol{\theta}_i}$ with respect to $\boldsymbol{\theta}_i$. Also, $\theta_i = \|\boldsymbol{\theta}_i\|$ denotes the norm of $\boldsymbol{\theta}_i$, $\boldsymbol{\rho}_i = \mathbf{R}_0^{i\top} [\mathbf{m}_k]_\times^\top \mathbf{b}_k$ denotes the residual vector, and $\text{sym}(\mathbf{A}) = (\mathbf{A} + \mathbf{A}^\top)/2$ finds the symmetric part of any square matrix \mathbf{A} .

The second part of the Hessian is when the index $i < j$, which is expressed as follows:

$$\frac{\partial^2 \mathcal{E}_m}{\partial \boldsymbol{\theta}_i \partial \boldsymbol{\theta}_j^\top} = \sum_{k \in \mathbb{K}, k \geq j} \mathbf{J}_{\mathbf{R}_l}^{\boldsymbol{\theta}_i} \mathbf{R}_0^{i\top} [\mathbf{b}_k]^\top [\mathbf{m}_k]_\times \mathbf{R}_0^j \mathbf{J}_{\mathbf{R}_r}^{\boldsymbol{\theta}_j}.$$

The third part is when the index $i > j$, expressed by

$$\begin{aligned} \frac{\partial^2 \mathcal{E}_m}{\partial \boldsymbol{\theta}_i \partial \boldsymbol{\theta}_j^\top} &= \sum_{k \in \mathbb{K}, k \geq i} \left(\mathbf{J}_{\mathbf{R}_l}^{\boldsymbol{\theta}_i} \mathbf{R}_0^{i\top} [\mathbf{b}_k]^\top [\mathbf{m}_k]_\times \mathbf{R}_0^j \mathbf{J}_{\mathbf{R}_r}^{\boldsymbol{\theta}_j} - \mathbf{J}_{\mathbf{R}_l}^{\boldsymbol{\theta}_i} \mathbf{R}_0^{i\top} [\mathbf{b}_k \times \mathbf{m}_k]^\top \mathbf{R}_0^j \mathbf{J}_{\mathbf{R}_r}^{\boldsymbol{\theta}_j} \right) \\ &= \sum_{k \in \mathbb{K}, k \geq i} \mathbf{J}_{\mathbf{R}_l}^{\boldsymbol{\theta}_i} \mathbf{R}_0^{i\top} [\mathbf{m}_k]^\top [\mathbf{b}_k]_\times \mathbf{R}_0^j \mathbf{J}_{\mathbf{R}_r}^{\boldsymbol{\theta}_j} \end{aligned}$$

which matches the transpose of the second part, as expected.

S.II. PROOF OF THEOREM AND LEMMA

A. Preliminary

The equilibrium equation of the MeSCR can be written as

$$\boldsymbol{\theta} = \boldsymbol{\Lambda}^{-1} \mathbf{M}(\boldsymbol{\theta}) \mathbf{b}. \quad (\text{S1})$$

Proposition 1. *The matrix-valued function $\mathbf{M}(\boldsymbol{\theta})$ and the magnetic torque $\mathbf{M}(\boldsymbol{\theta})\mathbf{b}$ are bounded on \mathbb{R}^{3N} with positive constants \mathcal{M}_0 and \mathcal{M} such that $\|\mathbf{M}(\boldsymbol{\theta})\| \leq \mathcal{M}_0$ and $\|\mathbf{M}(\boldsymbol{\theta})\mathbf{b}\| \leq \mathcal{M}$ for all $\boldsymbol{\theta} \in \mathbb{R}^{3N}$, respectively.*

Proposition 2. *The vector-valued function $\mathbf{M}(\boldsymbol{\theta})\mathbf{b}$ is Lipschitz continuous on \mathbb{R}^{3N} with a Lipschitz constant \mathcal{L} such that $\|\mathbf{M}(\boldsymbol{\theta})\mathbf{b} - \mathbf{M}(\boldsymbol{\varphi})\mathbf{b}\| \leq \mathcal{L}\|\boldsymbol{\theta} - \boldsymbol{\varphi}\|$ for all $\boldsymbol{\theta}, \boldsymbol{\varphi} \in \mathbb{R}^{3N}$.*

Theorem 1. *There exists a unique equilibrium solution to (S1) if the following inequality holds:*

$$\max_{k \in \mathbb{K}} B_k < \frac{\pi \lambda_{\min}(\boldsymbol{\Lambda})}{4 \sum_{k \in \mathbb{K}} k M_k} \quad (\text{S2})$$

where $\lambda_{\min}(\cdot)$ denotes the smallest eigenvalue of a matrix.

Lemma 1. *Let $\boldsymbol{\theta}^*$ be any equilibrium point of (S1). Using Proposition 1, we have $\|\boldsymbol{\theta}^*\| = \|\boldsymbol{\Lambda}^{-1} \mathbf{M}(\boldsymbol{\theta}^*) \mathbf{b}\| \leq \frac{\mathcal{M}}{\lambda_{\min}(\boldsymbol{\Lambda})}$.*

B. Theorem and Lemma Stated for Proof

Theorem 2. *The MeSCR is material-twist-free ($\boldsymbol{\theta}_i^\top \bar{\mathbf{t}}_i = 0$) for any actuating magnetic field, provided that the embedded magnets' magnetic moments are aligned axially, i.e., $\bar{\mathbf{m}}_k = \pm M_k \bar{\mathbf{t}}$, and the magnetic field strength satisfies:*

$$\max_{k \in \mathbb{K}} B_k \leq \frac{\sqrt{6} \lambda_{\min}(\boldsymbol{\Lambda})}{\sum_{k \in \mathbb{K}} M_k}. \quad (\text{S3})$$

Lemma 2. *Suppose the inequality condition in Theorem 1 holds. Then the immersion Jacobian admits the expansion*

$$\begin{aligned} \mathcal{J}_\theta^2 &= \det(\mathbf{U}_u^\top \mathbf{M}^\top \boldsymbol{\Lambda}^{-2} \mathbf{M} \mathbf{U}_u) + \epsilon \\ &\triangleq \tilde{\mathcal{J}}_\theta^2 + \epsilon \end{aligned} \quad (\text{S4})$$

where the remainder term ϵ is bounded above as

$$|\epsilon| \leq \frac{3(2\mathcal{L} - \mathcal{L}^2) N_m^3 \mathcal{M}_0^6}{(1 - \mathcal{L})^2 \Lambda_{\min}^6},$$

and satisfies $\lim_{B_k \rightarrow 0} |\epsilon| \rightarrow 0$.

C. Proof of Theorem 2

Proof. The gradient of the potential energy with respect to each joint angle ($\boldsymbol{\theta}_i$) can be rewritten as:

$$\begin{aligned} \nabla_{\boldsymbol{\theta}_i} \mathcal{E} &= \boldsymbol{\Lambda}_i \boldsymbol{\theta}_i - (\mathbf{R}_0^i \mathbf{J}_{\mathbf{R}_r}^{\boldsymbol{\theta}_i})^\top \sum_{k \in \mathbb{K}, k \geq i} [\mathbf{m}_k]_\times \mathbf{b}_k \\ &= \boldsymbol{\Lambda}_i \boldsymbol{\theta}_i - \mathbf{J}_{\mathbf{R}_l}^{\boldsymbol{\theta}_i} \sum_{k \in \mathbb{K}, k \geq i} \mathbf{R}_{i+1}^k \mathbf{v}_k \end{aligned} \quad (\text{S5})$$

where $\mathbf{v}_k = [\mathbf{R}_0^k \mathbf{b}_k]_\times^\top \bar{\mathbf{m}}_k$ is a vector perpendicular to the torsion axis ($\bar{\mathbf{t}}$) that $\forall k \in \mathbb{K}, \mathbf{v}_k^\top \bar{\mathbf{t}} = 0$. For the i th joint, the rotation matrix \mathbf{R}_{i+1}^k depends on its successor joints. Therefore, we propose a backward iteration method to solve the equilibrium solution.

Step 1: Analysis at the boundary joint

At the boundary joint with index $i = k_{N_m-1}$, where $\mathbf{R}_{i+1}^k = \mathbf{I}_3$, we denote $\mathbf{v}_{k_{N_m-1}}$ by \mathbf{v}_k for brevity. The left Jacobian associated with $\boldsymbol{\theta}_i$ can be expressed by

$$\mathbf{J}_{\mathbf{R}_i}^{\boldsymbol{\theta}_i} = \mathbf{I}_3 + \alpha[\boldsymbol{\theta}_i]_{\times} + \beta[\boldsymbol{\theta}_i]_{\times}^2 \quad (\text{S6})$$

where $0 < \alpha \leq \frac{1}{2}$ and $0 < \beta \leq \frac{1}{6}$ are bounded functions of $\boldsymbol{\theta}_i$. Substituting (S6) into (S5), we have:

$$\begin{aligned} \nabla_{\boldsymbol{\theta}_i} \mathcal{E} &= \boldsymbol{\Lambda}_i \boldsymbol{\theta}_i - (\mathbf{I}_3 + \alpha[\boldsymbol{\theta}_i]_{\times} + \beta[\boldsymbol{\theta}_i]_{\times}^2) \mathbf{v}_k \\ &= (\boldsymbol{\Lambda}_i - \alpha[\mathbf{v}_k]_{\times} - \beta \boldsymbol{\theta}_i^{\top} \mathbf{v}_k \mathbf{I}_3) \boldsymbol{\theta}_i - (1 - \beta \|\boldsymbol{\theta}_i\|^2) \mathbf{v}_k. \end{aligned} \quad (\text{S7})$$

The torsional component of (S7) can be obtained by taking the inner product with $\bar{\mathbf{t}}$, yielding:

$$\begin{aligned} \bar{\mathbf{t}}^{\top} \nabla_{\boldsymbol{\theta}_i} \mathcal{E} &= \bar{\mathbf{t}}^{\top} (\boldsymbol{\Lambda}_i - \alpha[\mathbf{v}_k]_{\times} - \beta \boldsymbol{\theta}_i^{\top} \mathbf{v}_k \mathbf{I}_3) \boldsymbol{\theta}_i \\ &= (\lambda_{\min}(\boldsymbol{\Lambda}_i) - \beta \boldsymbol{\theta}_i^{\top} \mathbf{v}_k) \bar{\mathbf{t}}^{\top} \boldsymbol{\theta}_i - \alpha (\bar{\mathbf{t}} \times \boldsymbol{\theta}_i)^{\top} \mathbf{v}_k. \end{aligned} \quad (\text{S8})$$

Step 2: Solution for $\boldsymbol{\theta}_i^*$ at the boundary joint

Let the solution of $\bar{\mathbf{t}}^{\top} \nabla_{\boldsymbol{\theta}_i} \mathcal{E} = 0$ be expressed as $\boldsymbol{\theta}_i^* = s_i \mathbf{v}_k + \mathbf{v}_k^{\perp}$, where $s_i \in \mathbb{R}$ is an undetermined scalar, and $\mathbf{v}_k^{\perp} \in \mathbb{R}^3$ is orthogonal to \mathbf{v}_k . Substituting into (S8), we derive the following system of equations:

$$\begin{cases} (\lambda_{\min}(\boldsymbol{\Lambda}_i) - s_i \beta \|\mathbf{v}_k\|^2) \bar{\mathbf{t}}^{\top} \mathbf{v}_k^{\perp} = 0, \\ \alpha \bar{\mathbf{t}}^{\top} [\mathbf{v}_k^{\perp}]_{\times} \mathbf{v}_k = 0. \end{cases}$$

From the above, the components of $\boldsymbol{\theta}_i^*$ can be determined as $s_i = \lambda_{\min}(\boldsymbol{\Lambda}_i) / (\beta \|\mathbf{v}_k\|^2)$ and $\mathbf{v}_k^{\perp} = \theta_t^i \bar{\mathbf{t}}$, where $\theta_t^i \in \mathbb{R}$ is arbitrary. We proceed to show that $\theta_t^i = 0$ under certain conditions. From Proposition 1, one has the inequality that $\|\mathbf{v}_k\| \leq \mathcal{M}_k$. Combining with $\beta \leq \frac{1}{6}$ and by Pythagoras' theorem reads

$$\|\boldsymbol{\theta}_i^*\|^2 = \|s_i \mathbf{v}_k\|^2 + \|\theta_t^i \bar{\mathbf{t}}\|^2 \geq \left(\frac{6 \lambda_{\min}(\boldsymbol{\Lambda}_i)}{\mathcal{M}_k} \right)^2 + \theta_t^i{}^2.$$

It is known from Lemma 1 that the norm of the equilibrium solution is bounded by $\mathcal{M}_k / \lambda_{\min}(\boldsymbol{\Lambda}_i)$, we obtain:

$$\theta_t^i{}^2 \leq \left(\frac{\mathcal{M}_k}{\lambda_{\min}(\boldsymbol{\Lambda}_i)} \right)^2 - \left(\frac{6 \lambda_{\min}(\boldsymbol{\Lambda}_i)}{\mathcal{M}_k} \right)^2. \quad (\text{S9})$$

Using the condition $\mathcal{M}_k \leq \sqrt{6} \lambda_{\min}(\boldsymbol{\Lambda}_i)$ derived from (S3), it follows that $\theta_t^i{}^2 \leq 0$. Therefore, the equilibrium solution simplifies to $\boldsymbol{\theta}_i^* = s_i \mathbf{v}_k$, whereas $\mathbf{v}_k^{\perp} = \mathbf{0}$. Substituting $\boldsymbol{\theta}_i^*$ into (S7), we find $s_i = 1 / \lambda_{\max}(\boldsymbol{\Lambda}_i)$.

Step 3: Recursive solution for inner joints

We now consider the next joint from backward, whose joint index $i = k_{N_m-1} - 1$. Using an important property of the rotation matrix that $\mathbf{R}(s\boldsymbol{\theta})\boldsymbol{\theta} = \boldsymbol{\theta}$ holds for any arbitrary constant s , we quickly notice

$$\mathbf{R}_{i+1}(\boldsymbol{\theta}_{i+1}^*) \mathbf{v}_k = \mathbf{R}_{i+1}(s_{i+1} \mathbf{v}_k) \mathbf{v}_k = \mathbf{v}_k.$$

Thus, the potential energy gradient of the current joint retains the same form as (S7), ensuring that $\boldsymbol{\theta}_i^*$ remains parallel to \mathbf{v}_k . Proceeding iteratively, we derive the general equilibrium solution:

$$\boldsymbol{\theta}_i^* = \frac{\sum_{k \geq i} \mathbf{v}_k}{\lambda_{\max}(\boldsymbol{\Lambda}_i)} = \frac{\sum_{k \geq i} [\mathbf{R}_0^{k \top}(\boldsymbol{\theta}^*) \mathbf{b}_k]_{\times}^{\top} \bar{\mathbf{m}}_k}{\lambda_{\max}(\boldsymbol{\Lambda}_i)}. \quad (\text{S10})$$

Although (S10) does not yield an explicit closed-form solution for $\boldsymbol{\theta}^*$, it nonetheless ensures that $\bar{\mathbf{t}}^{\top} \boldsymbol{\theta}_i^* = 0$, since $\mathbf{v}_k^{\top} \bar{\mathbf{t}} = 0$. This implies that the MeSCR is material-twist-free. \blacksquare

D. Proof of Lemma 2

Let $\mathbf{C} = \mathbf{M}(\boldsymbol{\theta})\mathbf{U}_u$ and $\mathbf{E} = \mathbf{C}^\top \boldsymbol{\Lambda}^{-2} \mathbf{C}$. Then the immersion Jacobian can be expressed as $\mathcal{J}_\theta^2 = \det(\mathbf{E} + \mathbf{F})$, where $\mathbf{F} = \mathbf{C}^\top (\mathbf{S}^{-2} - \boldsymbol{\Lambda}^{-2}) \mathbf{C}$. From Proposition 1, the following useful bounds hold:

$$\|\mathbf{C}\| \leq \sqrt{N_m} \mathcal{M}_0, \quad \|\mathbf{E}^{-1}\| \leq \frac{\Lambda_{\min}^2}{N_m \mathcal{M}_0^2}, \quad \det(\mathbf{E}) \leq \frac{N_m^3 \mathcal{M}_0^6}{\Lambda_{\min}^6}.$$

Noticing that the determinant admits the first-order expansion

$$\det(\mathbf{E} + \mathbf{F}) = \det(\mathbf{E}) (1 + \text{tr}(\mathbf{E}^{-1} \mathbf{F}) + \mathcal{O}(\|\mathbf{F}\|^2)),$$

which implies the following upper bound:

$$\begin{aligned} |\det(\mathbf{E} + \mathbf{F}) - \det(\mathbf{E})| &\lesssim \det(\mathbf{E}) |\text{tr}(\mathbf{E}^{-1} \mathbf{F})| \\ &\leq 3 \det(\mathbf{E}) \|\mathbf{E}^{-1}\| \|\mathbf{F}\|. \end{aligned} \quad (\text{S11})$$

Define the residual matrix $\mathbf{G} = \mathbf{S}^{-1} - \boldsymbol{\Lambda}^{-1}$, it reads $\mathbf{F} = \mathbf{C}^\top (\mathbf{G} \boldsymbol{\Lambda}^{-1} + \boldsymbol{\Lambda}^{-1} \mathbf{G} + \mathbf{G}^2) \mathbf{C}$. From Proposition 2 and under the condition $\|\boldsymbol{\Lambda}^{-1} \mathbf{S}_m\| < 1$, the residual satisfies the following bound derived from the Neumann series:

$$\|\mathbf{G}\| \leq \frac{\|\boldsymbol{\Lambda}^{-1} \mathbf{S}_m\| \|\boldsymbol{\Lambda}^{-1}\|}{1 - \|\boldsymbol{\Lambda}^{-1} \mathbf{S}_m\|} = \frac{\mathcal{L}}{\Lambda_{\min}(1 - \mathcal{L})}.$$

Hence, we can estimate $\|\mathbf{F}\|$ as follows:

$$\begin{aligned} \|\mathbf{F}\| &\leq \|\mathbf{C}^\top\| (2\|\mathbf{G}\| \|\boldsymbol{\Lambda}^{-1}\| + \|\mathbf{G}\|^2) \|\mathbf{C}\| \\ &= N_m \mathcal{M}_0^2 \frac{2\mathcal{L} - \mathcal{L}^2}{\Lambda_{\min}^2 (1 - \mathcal{L})^2}. \end{aligned} \quad (\text{S12})$$

Substituting (S12) into (S11), we obtain

$$|\epsilon| = |\det(\mathbf{E} + \mathbf{F}) - \det(\mathbf{E})| \leq 3 \frac{N_m^3 \mathcal{M}_0^6}{\Lambda_{\min}^6} \frac{2\mathcal{L} - \mathcal{L}^2}{(1 - \mathcal{L})^2},$$

as claimed. Finally, since $\mathcal{L} \rightarrow 0$ as $B_k \rightarrow 0$, it follows that $|\epsilon| \rightarrow 0$ in this limit.